



HAL
open science

Equilibrated warping: Finite element image registration with finite strain equilibrium gap regularization

Martin Genet, C. T Stoeck, C. von Deuster, L. C. Lee, S. Kozerke

► To cite this version:

Martin Genet, C. T Stoeck, C. von Deuster, L. C. Lee, S. Kozerke. Equilibrated warping: Finite element image registration with finite strain equilibrium gap regularization. *Medical Image Analysis*, 2018, 50, pp.1-22. 10.1016/j.media.2018.07.007 . hal-01882366

HAL Id: hal-01882366

<https://hal.science/hal-01882366v1>

Submitted on 27 Sep 2018

HAL is a multi-disciplinary open access archive for the deposit and dissemination of scientific research documents, whether they are published or not. The documents may come from teaching and research institutions in France or abroad, or from public or private research centers.

L'archive ouverte pluridisciplinaire **HAL**, est destinée au dépôt et à la diffusion de documents scientifiques de niveau recherche, publiés ou non, émanant des établissements d'enseignement et de recherche français ou étrangers, des laboratoires publics ou privés.

Equilibrated Warping: Finite Element Image Registration with Finite Strain Equilibrium Gap Regularization

M. Genet^{a,b,*}, C. T. Stoeck^c, C. von Deuster^c, L. C. Lee^d, S. Kozerke^c

^a*Laboratoire de Mécanique des Solides, École Polytechnique / C.N.R.S. / Université Paris-Saclay,
Palaiseau, France*

^b*M3DISIM team, Inria / Université Paris-Saclay, Palaiseau, France*

^c*Institute for Biomedical Engineering, University and ETH Zurich, Switzerland*

^d*Department of Mechanical Engineering, Michigan State University, East Lansing, USA*

Abstract

In this paper, we propose a novel continuum finite strain formulation of the equilibrium gap regularization for image registration. The equilibrium gap regularization essentially penalizes any deviation from the solution of a hyperelastic body in equilibrium with arbitrary loads prescribed at the boundary. It thus represents a regularization with strong mechanical basis, especially suited for cardiac image analysis. We describe the consistent linearization and discretization of the regularized image registration problem, in the framework of the finite elements method. The method is implemented using FEniCS & VTK, and distributed as a freely available python library. We show that the equilibrated warping method is effective and robust: regularization strength and image noise have minimal impact on motion tracking, especially when compared to strain-based regularization methods such as hyperelastic warping. We also show that equilibrated warping is able to extract main deformation features on both tagged and untagged cardiac magnetic resonance images.

Highlights.

- Continuum finite strain formulation of the equilibrium gap regularization principle
- Consistent linearization and finite element discretization
- Efficient implementation based on FEniCS & VTK, freely available as a python library
- Equilibrium gap regularization allows the registration of highly noisy images
- Equilibrated warping can extract strains from cardiac magnetic resonance images

Keywords:

Finite elements, Image registration, Equilibrium gap regularization, Cardiac magnetic resonance imaging

*Corresponding author. martin.genet@polytechnique.edu

1	Contents	
2	1 Introduction	2
3	2 Methods	4
4	2.1 Finite element-based image registration	4
5	2.1.1 Problem	4
6	2.1.2 Resolution	6
7	2.1.3 Implementation	9
8	2.2 Image synthesis, acquisition, combination and segmentation	10
9	2.2.1 Image synthesis	10
10	2.2.2 Image acquisition and combination	11
11	2.2.3 Image segmentation	12
12	3 Results & Discussion	13
13	3.1 Validation on <i>in silico</i> images	13
14	3.1.1 Influence of regularization strength	13
15	3.1.2 Influence of mesh density	16
16	3.2 Results on <i>in vivo</i> images	16
17	3.2.1 Results on <i>in vivo</i> tagged images	16
18	3.2.2 Results on <i>in vivo</i> untagged images	18
19	3.3 Limitations	24
20	4 Conclusion	24
21	Appendix A Validation using Motion Tracking Challenge	28
22	Appendix B Vitae	28
23	Appendix B.1 Martin Genet	28
24	Appendix B.2 Christian Stoeck	29
25	Appendix B.3 Constantin von Deuster	29
26	Appendix B.4 Lik Chuan Lee	29
27	Appendix B.5 Sebastian Kozerke	29
28	References	30
29	<hr/>	

30 **1. Introduction**

31 Image processing, in particular image registration for motion tracking, is playing an
32 important role in biomedical imaging [Tobon-Gomez et al., 2013; Sotiras et al., 2013] and
33 in other domains such as materials and mechanical engineering [Sutton and Hild, 2015].
34 However, despite important progress made in the past decades, robustness, efficiency and
35 precision of the existing methods must still be improved to translate them into medical

1 and engineering applications. In this paper we propose a novel regularization approach
2 that has a strong mechanical basis, and apply it to finite element-based image registration
3 problems. We illustrate our approach on cardiac motion tracking from magnetic resonance
4 (MR) images.

5 MR imaging (MRI) is a powerful tool that can be used to quantify the motion of the beat-
6 ing heart *in vivo* and non-invasively, with wide ranging clinical applications. They include
7 the diagnosis of coronary artery diseases, myocardial ischemia and infarction, non-ischemic
8 cardiomyopathies, ventricular dyssynchrony, *etc.* [Shehata et al., 2009; Ibrahim, 2011]. Be-
9 sides diagnosing heart diseases, cardiac motion tracking is also used as a component of other
10 MRI techniques, for instance in *in vivo* diffusion tensor imaging [Stoeck et al., 2015; von
11 Deuster et al., 2015], which has high clinical relevance. In the field of personalized compu-
12 tational modeling [Krishnamurthy et al., 2013; Lee et al., 2014], cardiac motion tracking is
13 used to estimate model parameters that could serve as biomarkers for cardiovascular diseases
14 [Sermesant et al., 2006; Imperiale et al., 2011].

15 Since regular anatomical cine MR images have little contrast within the myocardial wall,
16 tagged MRI was designed to track material points through the generation and imaging
17 of a magnetization grid (SPAtial Modulation of Magnetization, SPAMM) [Zerhouni et al.,
18 1988; Axel and Dougherty, 1989]. It was later improved with the Complementary SPAMM
19 (CSPAMM) method, which prevents tag fading [Fischer et al., 1993]. Accelerated whole-
20 heart 3D sequences (3D CSPAMM) have since been proposed [Ryf et al., 2002], which
21 mitigate misregistration issues common with multi-slice acquisitions and allow for fast and
22 reliable tracking of the entire left ventricle throughout the cardiac cycle (except for end-
23 diastole) in only three [Rutz et al., 2008], or even a single [Stoeck et al., 2012] breath hold.

24
25 Multiple approaches have been proposed to post-process cardiac magnetic resonance
26 images and extract motion and deformation fields [Wang and Amini, 2012; Tobon-Gomez
27 et al., 2013]. They vary in the nature of the *a priori* knowledge that is used to better
28 distinguish signal from noise, and how it is incorporated. A first distinction exists between
29 data assimilation and image registration techniques. In data assimilation, a realistic physical
30 model is used and its parameters are estimated to best match the acquired images [Sermesant
31 et al., 2006; Sainte-Marie et al., 2006]. This estimation is either variational [Delingette et al.,
32 2012] or sequential [Moireau et al., 2008; Chapelle et al., 2013]. In other communities, this
33 is called integrated image correlation [Hild and Roux, 2006; Hild et al., 2016]. Conversely,
34 in image registration techniques, which are the focus of this paper, only limited *a priori*
35 knowledge is required, solely to regularize the registration problem. The strengths and
36 weaknesses of both approaches are opposite: using a realistic model as regularizer allows to
37 process low resolution and/or noisy data while extracting meaningful physical parameters;
38 on the other hand the processing is highly dependent on the validity of the model.

39 Within image registration methods, another distinction exists, between Fourier-based
40 and tracking-based methods [Tobon-Gomez et al., 2013]. Among Fourier-based methods,
41 HARMonic Phases (HARP)-based techniques [Osman et al., 1999; Garot et al., 2000] are
42 the most commonly used methods, which have enabled fully automatic post-processing of
43 tagged images. Based on similar concepts, the SinMod method [Arts et al., 2010; Wang

1 et al., 2013] offers improved motion tracking performance. However, these methods are
2 limited to tagged images, as HARP requires phase data, and SinMod makes use of the sine
3 modulation of magnitude data. In contrast, tracking-based methods, which are the focus of
4 this paper, can be applied to any type of images.

5 A final notable distinction exists, within tracking-based image registration techniques,
6 between local and global approaches [Hild and Roux, 2012]. In local approaches, images
7 are correlated region by region [Lenoir et al., 2007], while in global approaches they are
8 correlated at once [Veress et al., 2005; Phatak et al., 2009]. Note that hybrid methods have
9 been proposed, which efficiently alternate between local and global steps [Thirion, 1998;
10 Vercauteren et al., 2008].

11
12 The present paper focuses on global tracking-based image registration, specifically on
13 the regularization of the registration problem. Basic mathematical regularization such as
14 Laplacian smoothing [Passieux and Périé, 2012] penalizes rigid body rotations and are thus
15 limited to very small deformations. Fluid-like mechanical regularization has been proposed
16 in [Christensen et al., 1996], which is not suitable for the (solid) myocardium as it does not
17 enforce the continuity of the displacement field. Incompressibility has also been used as a
18 regularizer [Mansi et al., 2011; McLeod et al., 2012], but it represents a strong kinematic
19 constraint that can potentially interfere with the estimation of the actual kinematics de-
20 scribed in the images. Hyperelastic regularization [Veress et al., 2005; Phatak et al., 2009;
21 Burger et al., 2013] uses a proper strain measure valid for arbitrary large rotations and
22 deformations, but still penalizes strain itself, hence might be considered too strong of a
23 regularization as well.

24 In this paper, we propose a novel regularizer for finite element-based image registration
25 problems based on the continuum finite strain formulation of the equilibrium gap principle.
26 This regularizer has strong physical basis as it penalizes any deviation from the mechanical
27 equilibrium (which is a fundamental principle) instead of penalizing the kinematics itself
28 (which can be arbitrary). It also benefits from the finite elasticity framework, and does not
29 penalize rigid body displacement or rotation. This work inherits ideas from [Claire et al.,
30 2004; Leclerc et al., 2010], where a similar regularizer has been formulated at the discrete
31 level, and within the linearized elasticity framework. The formulation is presented in details
32 in Section 2, validation is provided in Section 3.1, and an illustration on *in vivo* cardiac MR
33 images is given in Section 3.2.

34 2. Methods

35 2.1. Finite element-based image registration

36 2.1.1. Problem

37 *Formulation.* Let us denote I_0 & I_t as the scalar intensity fields of two images representing
38 an object occupying the domains Ω_0 & Ω_t in the reference and deformed states, respectively.
39 The problem is to find the smooth mapping $\underline{\varphi}$, or equivalently the smooth displacement field
40 \underline{U} ($\underline{\varphi}(\underline{X}) = \underline{X} + \underline{U}(\underline{X})$), between Ω_0 & Ω_t . This problem is ill-posed, notably because of

1 image noise, and must thus be formulated as a regularized minimization problem:

$$\text{find } \underline{U} = \operatorname{argmin}_{\{\underline{U}^*\}} \{J(\underline{U}^*) = (1 - \beta) \Psi^{\text{im}}(\underline{U}^*) + \beta \Psi^{\text{reg}}(\underline{U}^*)\}, \quad (1)$$

2 where J is the functional to minimize, Ψ^{im} the image similarity metric or “energy”, Ψ^{reg} the
3 regularization “energy”, and β is the regularization strength.

4 *Similarity metric.* We use a simple sum of squares between image intensities, written here
5 in the reference configuration, as similarity metric:

$$\Psi^{\text{im}}(\underline{U}^*) = \frac{1}{2} \int_{\Omega_0} (I_t(\underline{X} + \underline{U}^*(\underline{X})) - I_0(\underline{X}))^2 d\Omega_0 = \frac{1}{2} \int_{\Omega_0} (I_t \circ \underline{\varphi}^* - I_0)^2 d\Omega_0. \quad (2)$$

6 *Regularization.* Many regularizers have been proposed for image registration problems, in-
7 cluding fluid [Christensen et al., 1996] and hyperelastic [Veress et al., 2005; Phatak et al.,
8 2009; Genet et al., 2016] constraints.

9 In hyperelastic warping [Veress et al., 2005; Phatak et al., 2009], the regularization energy
10 is directly the strain energy of the body:

$$\Psi^{\text{reg,hyper}} = \int_{\Omega_0} \rho_0 \psi d\Omega_0, \quad (3)$$

11 where ρ_0 is the mass density, and ψ the specific strain energy potential. Thus, strain, a
12 quantity that we seek to extract from the images and that can be in principle arbitrary, is
13 directly penalized by the regularization in hyperelastic warping. Moreover, the minimizer of
14 Problem (1-3), being the minimum of a “potential” energy, is the solution of a mechanical
15 problem of a body in equilibrium under an unphysical body force that corresponds to the
16 mismatch between the image intensity fields. The obtained deformation therefore has weak
17 mechanical basis.

18 Motivated by this inconsistency, we propose an alternate regularizer, which essentially
19 penalizes any deviation from the solution of a hyperelastic body in equilibrium with arbitrary
20 boundary loads (but no body load). Let us first recall that mechanical equilibrium, *i.e.*,
21 conservation of momentum, in absence of body load and inertia, can be expressed as:

$$\begin{cases} \operatorname{Div}(\underline{F} \cdot \underline{S}) = 0 \\ {}^t \underline{S} = \underline{S} \end{cases} \quad \forall \underline{X} \in \Omega_0, \quad (4)$$

22 where \underline{S} is the second Piola-Kirchhoff stress tensor, and $\underline{F} = \frac{\partial \underline{\varphi}}{\partial \underline{X}}$ the transformation gradient
23 [Holzapfel, 2000]. These relations correspond to conservation of linear and angular momen-
24 tum, respectively. We also recall that the second principle of thermodynamics requires that:

$$\underline{S} = \frac{\partial \rho_0 \psi}{\partial \underline{E}}, \quad (5)$$

26 where $\underline{E} = \frac{1}{2}(\underline{C} - \underline{1})$ is the Green-Lagrange strain tensor, and $\underline{C} = {}^t \underline{F} \cdot \underline{F}$ the right Cauchy-
27 Green dilatation tensor [Holzapfel, 2000]. The Green-Lagrange strain tensor is symmetric,

1 such that when computed through the constitutive law (5) the second Piola-Kirchhoff stress
2 tensor is necessarily symmetric, and the conservation of angular momentum is automatically
3 verified. However, the conservation of linear momentum still needs to be enforced. In
4 principle one could use $\Psi^{\text{reg, equil}} = \frac{1}{2} \|\text{Div}(\underline{\underline{F}} \cdot \underline{\underline{S}})\|_{L^2(\Omega_0)}^2$. However, we discretize Problem
5 (1) using standard Lagrange elements, so that $\underline{\underline{F}}$ and $\underline{\underline{S}}$ belong to $L^2(\Omega_0)$ —more strictly they
6 belong to piecewise- $H(\text{div}; \Omega_0)$, but not to $H(\text{div}; \Omega_0)$, as they are $H(\text{div})$ on the elements
7 but have jumps across element faces. Thus, the following equivalent norm is used instead:

$$\Psi^{\text{reg, equil}} = \sum_K \frac{1}{2} \|\text{Div}(\underline{\underline{F}} \cdot \underline{\underline{S}})\|_{L^2(K)}^2 + \sum_F \frac{1}{2h} [[\underline{\underline{F}} \cdot \underline{\underline{S}} \cdot \underline{\underline{N}}]]_{L^2(F)}^2, \quad (6)$$

8 where K denotes the set of elements, F the set the interior faces with normal $\underline{\underline{N}}$, and h a
9 characteristic length of the finite element mesh. When the mesh is refined, if the discrete
10 stress field converges toward a continuous solution, this discrete norm converges toward
11 the original continuous norm. This regularization is an extension of the equilibrium gap
12 regularization [Claire et al., 2004], but written at the continuous level and valid for arbitrary
13 large deformations.

14 *Mechanical model.* As strain energy potential, for both hyperelastic and equilibrated warping
15 we use the classical Ciarlet-Geymonat potential:

$$\rho_0 \psi = \frac{\kappa}{2} (J^2 - 1 - \ln(J)) + \frac{\mu}{2} (I_C - 3 - 2 \ln(J)), \quad (7)$$

16 where κ & μ denote bulk and shear modulus, $J = \det(\underline{\underline{F}})$, $I_C = \text{tr}(\underline{\underline{C}})$, $\underline{\underline{C}} = {}^t \underline{\underline{F}} \cdot \underline{\underline{F}}$,
17 $\underline{\underline{F}} = \underline{\underline{1}} + \underline{\underline{\text{Grad}}}(\underline{\underline{U}})$ [Ciarlet and Geymonat, 1982]. Contrary to the Saint Venant-Kirchhoff
18 potential, the Ciarlet-Geymonat potential is valid for arbitrary deformation levels [Ciarlet
19 and Geymonat, 1982; Le Tallec, 1994]. In practice, we use a unit Young's modulus and null
20 Poisson's ratio, which is equivalent to $\kappa = \frac{1}{3}$ & $\mu = \frac{1}{2}$, the strength of the regularization
21 being set by the parameter β .

22 Let us point out that an incompressible material law could be used to enforce incompress-
23 ibility. However, that would represent too strong of a kinematic constraint for a problem
24 whose aim is to extract the kinematics from images. Moreover, it is known that the my-
25 ocardial deformation is not fully incompressible, notably because of perfusion effects [May-
26 Newman et al., 1994]. Nevertheless, if the deformation is indeed incompressible, and that is
27 well represented in the images, the current regularization will not interfere with the image
28 registration, even with a Poisson's ratio of 0. Indeed, the surface loads will simply adapt
29 themselves so that the deformation of the mesh matches the one in the images.

30 2.1.2. Resolution

31 *Variational formulation.* The first variation of Problem (1) yields its variational formulation:

$$\text{find } \underline{\underline{U}} \quad / \quad D_{\underline{\underline{V}}} J(\underline{\underline{U}}) = (1 - \beta) D_{\underline{\underline{V}}} \Psi^{\text{im}}(\underline{\underline{U}}) + \beta D_{\underline{\underline{V}}} \Psi^{\text{reg}}(\underline{\underline{U}}) = 0 \quad \forall \underline{\underline{V}}, \quad (8)$$

1 where

$$D_{\underline{V}}\Psi^{\text{im}}(\underline{U}) = \int_{\Omega_0} (I_t \circ \underline{\varphi} - I_0) (\nabla I_t \circ \underline{\varphi} \cdot \underline{V}) d\Omega_0 \quad (9)$$

2 For the case of hyperelastic warping, one obtains:

$$D_{\underline{V}}\Psi^{\text{reg,hyper}}(\underline{U}) = \int_{\Omega_0} \frac{\partial \rho_0 \psi}{\partial \underline{E}}(\underline{U}) : \underline{\delta E}(\underline{U}, \underline{V}) d\Omega_0, \quad (10)$$

3 where $\underline{\delta E}(\underline{U}, \underline{V}) = (\underline{F}(\underline{U}) \cdot \underline{\text{Grad}}(\underline{V}))_{\text{sym}}$ denotes the variation of Green-Lagrange strain
4 [Holzapfel, 2000]. For the case of equilibrated warping, the following expression results:

$$\begin{aligned} D_{\underline{V}}\Psi^{\text{reg, equil}}(\underline{U}) &= \sum_K \int_K \underline{\text{Div}} \left(\underline{F}(\underline{U}) \cdot \frac{\partial \rho_0 \psi}{\partial \underline{E}}(\underline{U}) \right) \\ &\quad \cdot \underline{\text{Div}} \left(\underline{\text{Grad}}(\underline{V}) \cdot \frac{\partial \rho_0 \psi}{\partial \underline{E}}(\underline{U}) + \underline{F}(\underline{U}) \cdot \left(\frac{\partial^2 \rho_0 \psi}{\partial \underline{E}^2}(\underline{U}) : \underline{\delta E}(\underline{U}, \underline{V}) \right) \right) dK \\ &+ \sum_F \int_F \left[\left[\left(\underline{F}(\underline{U}) \cdot \frac{\partial \rho_0 \psi}{\partial \underline{E}}(\underline{U}) \right) \cdot \underline{N} \right] \right. \\ &\quad \left. \cdot \left[\left[\left(\underline{\text{Grad}}(\underline{V}) \cdot \frac{\partial \rho_0 \psi}{\partial \underline{E}}(\underline{U}) + \underline{F}(\underline{U}) \cdot \left(\frac{\partial^2 \rho_0 \psi}{\partial \underline{E}^2}(\underline{U}) : \underline{\delta E}(\underline{U}, \underline{V}) \right) \right) \cdot \underline{N} \right] \right] dF. \end{aligned} \quad (11)$$

5
6 *Linearization.* Nonlinear Problem (8) is solved iteratively using Newton's method, so that
7 at each iteration the following linearized problem must be solved:

$$\begin{aligned} \text{find } \underline{\Delta U} \quad / \quad (1 - \beta) a^{\text{im}}(\underline{U}; \underline{\Delta U}, \underline{V}) + \beta a^{\text{reg}}(\underline{U}; \underline{\Delta U}, \underline{V}) \\ = (1 - \beta) b^{\text{im}}(\underline{U}; \underline{V}) + \beta b^{\text{reg}}(\underline{U}; \underline{V}) \quad \forall \underline{V}, \end{aligned} \quad (12)$$

8 where (without image Hessian terms)

$$\begin{cases} a^{\text{im}}(\underline{U}; \underline{\Delta U}, \underline{V}) = \int_{\Omega_0} ((\nabla I_t \circ \underline{\varphi}(\underline{U})) \cdot \underline{\Delta U}) ((\nabla I_t \circ \underline{\varphi}(\underline{U})) \cdot \underline{V}) d\Omega_0 \\ b^{\text{im}}(\underline{U}; \underline{V}) = \int_{\Omega_0} ((I_t \circ \underline{\varphi}(\underline{U})) - I_0) ((\nabla I_t \circ \underline{\varphi}(\underline{U})) \cdot \underline{V}) d\Omega_0 \end{cases} . \quad (13)$$

9 For the case of hyperelastic warping, one has:

$$\begin{cases} a^{\text{reg,hyper}}(\underline{U}; \underline{\Delta U}, \underline{V}) = \int_{\Omega_0} \frac{\partial \rho_0 \psi}{\partial \underline{E}}(\underline{U}) : \underline{\delta E}(\underline{\Delta U}, \underline{V}) \\ \quad + \underline{\delta E}(\underline{U}, \underline{\Delta U}) : \frac{\partial^2 \rho_0 \psi}{\partial \underline{E}^2}(\underline{U}) : \underline{\delta E}(\underline{U}, \underline{V}) d\Omega_0 \\ b^{\text{reg,hyper}}(\underline{U}; \underline{V}) = \int_{\Omega_0} \frac{\partial \rho_0 \psi}{\partial \underline{E}}(\underline{U}) : \underline{\delta E}(\underline{U}, \underline{V}) d\Omega_0 \end{cases} . \quad (14)$$

1 And for the case of equilibrated warping, one obtains:

$$\left(\begin{aligned}
& a^{\text{reg, equil}}(\underline{U}; \underline{\Delta U}, \underline{V}) = \sum_K \int_K \left(\text{Div} \left(\underline{\text{Grad}}(\underline{\Delta U}) \cdot \frac{\partial \rho_0 \psi}{\partial \underline{E}}(\underline{U}) + \underline{F}(\underline{U}) \cdot \left(\frac{\partial^2 \rho_0 \psi}{\partial \underline{E}^2}(\underline{U}) : \underline{\delta E}(\underline{U}, \underline{\Delta U}) \right) \right) \right. \\
& \quad \cdot \text{Div} \left(\underline{\text{Grad}}(\underline{V}) \cdot \frac{\partial \rho_0 \psi}{\partial \underline{E}}(\underline{U}) + \underline{F}(\underline{U}) \cdot \left(\frac{\partial^2 \rho_0 \psi}{\partial \underline{E}^2}(\underline{U}) : \underline{\delta E}(\underline{U}, \underline{V}) \right) \right) \\
& \quad + \text{Div} \left(\underline{F}(\underline{U}) \cdot \frac{\partial \rho_0 \psi}{\partial \underline{E}}(\underline{U}) \right) \\
& \quad \cdot \text{Div} \left(\underline{\text{Grad}}(\underline{V}) \cdot \left(\frac{\partial^2 \rho_0 \psi}{\partial \underline{E}^2}(\underline{U}) : \underline{\delta E}(\underline{U}, \underline{\Delta U}) \right) + \underline{\text{Grad}}(\underline{\Delta U}) \cdot \left(\frac{\partial^2 \rho_0 \psi}{\partial \underline{E}^2}(\underline{U}) : \underline{\delta E}(\underline{U}, \underline{V}) \right) \right. \\
& \quad \left. \left. + \underline{F}(\underline{U}) \cdot \left(\underline{\delta E}(\underline{U}, \underline{\Delta U}) : \frac{\partial^3 \rho_0 \psi}{\partial \underline{E}^3}(\underline{U}) : \underline{\delta E}(\underline{U}, \underline{V}) + \frac{\partial^2 \rho_0 \psi}{\partial \underline{E}^2}(\underline{U}) : \underline{\delta \delta E}(\underline{\Delta U}, \underline{V}) \right) \right) \right) dK \\
& + \sum_F \int_F \left[\left[\left(\underline{\text{Grad}}(\underline{\Delta U}) \cdot \frac{\partial \rho_0 \psi}{\partial \underline{E}}(\underline{U}) + \underline{F}(\underline{U}) \cdot \left(\frac{\partial^2 \rho_0 \psi}{\partial \underline{E}^2}(\underline{U}) : \underline{\delta E}(\underline{U}, \underline{\Delta U}) \right) \right) \cdot \underline{N} \right] \right. \\
& \quad \left. \cdot \left[\left[\left(\underline{\text{Grad}}(\underline{V}) \cdot \frac{\partial \rho_0 \psi}{\partial \underline{E}}(\underline{U}) + \underline{F}(\underline{U}) \cdot \left(\frac{\partial^2 \rho_0 \psi}{\partial \underline{E}^2}(\underline{U}) : \underline{\delta E}(\underline{U}, \underline{V}) \right) \right) \cdot \underline{N} \right] \right] \right. \\
& + \left[\left[\left(\underline{F}(\underline{U}) \cdot \frac{\partial \rho_0 \psi}{\partial \underline{E}}(\underline{U}) \right) \cdot \underline{N} \right] \right. \\
& \quad \left. \cdot \left[\left[\left(\underline{\text{Grad}}(\underline{V}) \cdot \left(\frac{\partial^2 \rho_0 \psi}{\partial \underline{E}^2}(\underline{U}) : \underline{\delta E}(\underline{U}, \underline{\Delta U}) \right) + \underline{\text{Grad}}(\underline{\Delta U}) \cdot \left(\frac{\partial^2 \rho_0 \psi}{\partial \underline{E}^2}(\underline{U}) : \underline{\delta E}(\underline{U}, \underline{V}) \right) \right) \right. \right. \right. \\
& \quad \left. \left. \left. + \underline{F}(\underline{U}) \cdot \left(\underline{\delta E}(\underline{U}, \underline{\Delta U}) : \frac{\partial^3 \rho_0 \psi}{\partial \underline{E}^3}(\underline{U}) : \underline{\delta E}(\underline{U}, \underline{V}) + \frac{\partial^2 \rho_0 \psi}{\partial \underline{E}^2}(\underline{U}) : \underline{\delta \delta E}(\underline{\Delta U}, \underline{V}) \right) \right) \cdot \underline{N} \right] \right] dF \\
& b^{\text{reg, equil}}(\underline{U}; \underline{V}) = \sum_K \int_K \text{Div} \left(\underline{F}(\underline{U}) \cdot \frac{\partial \rho_0 \psi}{\partial \underline{E}}(\underline{U}) \right) \\
& \quad \cdot \text{Div} \left(\underline{\text{Grad}}(\underline{V}) \cdot \frac{\partial \rho_0 \psi}{\partial \underline{E}}(\underline{U}) + \underline{F}(\underline{U}) \cdot \left(\frac{\partial^2 \rho_0 \psi}{\partial \underline{E}^2}(\underline{U}) : \underline{\delta E}(\underline{U}, \underline{V}) \right) \right) dK \\
& \quad + \sum_F \int_F \left[\left[\left(\underline{F}(\underline{U}) \cdot \frac{\partial \rho_0 \psi}{\partial \underline{E}}(\underline{U}) \right) \cdot \underline{N} \right] \right. \\
& \quad \left. \cdot \left[\left[\left(\underline{\text{Grad}}(\underline{V}) \cdot \frac{\partial \rho_0 \psi}{\partial \underline{E}}(\underline{U}) + \underline{F}(\underline{U}) \cdot \left(\frac{\partial^2 \rho_0 \psi}{\partial \underline{E}^2}(\underline{U}) : \underline{\delta E}(\underline{U}, \underline{V}) \right) \right) \cdot \underline{N} \right] \right] dF
\end{aligned} \right) \tag{15}$$

2 where $\underline{\delta \delta E}(\underline{\Delta U}, \underline{V}) = ({}^t \underline{\text{Grad}}(\underline{\Delta U}) \cdot \underline{\text{Grad}}(\underline{V}))_{\text{sym}}$ denotes the second variation of Green-
3 Lagrange strain [Holzapfel, 2000].

4 *Discretization.* Problem (12) is discretized using standard continuous Galerkin elements,
5 yielding the discrete problem:

$$\text{find } \underline{\Delta U} \quad / \quad ((1 - \beta) \underline{\mathbb{A}}^{\text{im}}(\underline{U}) + \beta \underline{\mathbb{A}}^{\text{reg}}(\underline{U})) \cdot \underline{\Delta U} = (1 - \beta) \underline{\mathbb{B}}^{\text{im}}(\underline{U}) + \beta \underline{\mathbb{B}}^{\text{reg}}(\underline{U}) \tag{16}$$

6 *Nonlinear solver.* For a given couple of images, the discrete Problem (16) is iterated un-
7 til convergence. In practice, convergence is achieved when the incremental error (*i.e.*,
8 $\|\underline{\Delta U}\|/\|\underline{U}\|$) reaches 1%. For time series of images, each image t is registered to the ref-
9 erence image 0, taking the converged solution of the previous image $t - 1$ as initialization of
10 the nonlinear iterations for the current image t .

1 *Gradient-free line search.* The solution of Problem (8) has proven unstable, especially on *in*
2 *vivo* images, notably (i) because of the steepness of the mechanical term, and (ii) because
3 in the current VTK implementation, interpolated gradients are not the actual gradients
4 of the interpolated images¹ (so that the minimum of the image similarity energy does not
5 correspond to the root of its “derivative”). Thus, a gradient-free golden section line search
6 [Press et al., 2007] has been implemented, where the initial interval is taken as $\left[\frac{1-\varphi}{2-\varphi}, \frac{1}{2-\varphi}\right]$
7 (with $\varphi = \frac{1+\sqrt{5}}{2}$) such that the two initially tested values are 0 & 1. This line search comes
8 after the search direction as been computed by solving Problem (16), and allows to find the
9 optimal relaxation parameter at each iteration.

10 *Image scaling.* Since the image norm used here is sensitive to global image intensity that
11 changes from scan to scan and, for tagged images, that decreases slowly throughout the
12 cardiac cycle, we introduce a global image intensity scaling. Because the decrease is slow,
13 we use an explicit scaling. Specifically, after registering the image t to the reference image
14 0, we compute the linear scaling that best matches both images:

$$\text{find } (a, b) = \operatorname{argmin}_{\mathbb{R}^2} \left\{ J^2(a^*, b^*) = \frac{1}{2} \int_{\Omega_0} ((a^* (I_t \circ \underline{\varphi}) + b^*) - I_0)^2 d\Omega_0 \right\}, \quad (17)$$

15 which leads to the following symmetric linear system:

$$\begin{pmatrix} \int_{\Omega_0} (I_t \circ \underline{\varphi})^2 d\Omega_0 & \int_{\Omega_0} (I_t \circ \underline{\varphi}) d\Omega_0 \\ \int_{\Omega_0} (I_t \circ \underline{\varphi}) d\Omega_0 & 1 \end{pmatrix} \cdot \begin{pmatrix} a \\ b \end{pmatrix} = \begin{pmatrix} \int_{\Omega_0} I_0 \cdot (I_t \circ \underline{\varphi}) d\Omega_0 \\ \int_{\Omega_0} I_0 d\Omega_0 \end{pmatrix} \quad (18)$$

16 This scaling is then used for the registration of the subsequent image $t + 1$ to the reference
17 image 0.

18 2.1.3. Implementation

19 The time stepping, nonlinear solver and gradient-free line search have been implemented
20 in python². The finite element procedure is directly based on the FEniCS library³, which
21 provides automatic derivation and integration of the mechanical terms (14) or (15): as
22 FEniCS can process symbolic expressions, it can determine the degree of the expressions
23 it is given, and thus determine the order of the quadrature required to exactly integrate
24 these expressions [Logg et al., 2012; Alnæs et al., 2015]. Integration of image terms (13) is
25 done with the help of the VTK library⁴ for image derivation and interpolation [Schroeder
26 et al., 2006], using linear interpolation of image intensity and image gradients. High-order
27 quadrature is used for integration of image terms, in order to have as many integration

¹http://www.vtk.org/Wiki/VTK/Image_Interpolators#Gradients

²<https://www.python.org>

³<https://www.fenicsproject.org>

⁴<http://www.vtk.org>

1 points as pixels in the mesh. For greater efficiency, the C++ interface to both FEniCS &
 2 VTK is used for the integration of image terms. The code is freely available at https://gitlab.inria.fr/mgenet/dolfin_dic.

4 2.2. Image synthesis, acquisition, combination and segmentation

5 2.2.1. Image synthesis

6 In order to validate our method, we generated a series of 2D synthetic tagged MR images.
 7 The reference image has the following intensity field:

$$I_0(\underline{X}) = \sqrt{\left| \sin\left(\frac{\pi X_0}{s}\right) \right| \cdot \left| \sin\left(\frac{\pi X_1}{s}\right) \right|}, \quad (19)$$

8 where X_0 & X_1 denote spatial coordinates, and s is the tagging period. The prescribed
 9 deformation is a simple uniaxial and uniform deformation:

$$\begin{cases} x_0 = \sqrt{2f(t) + 1} X_0 \\ x_1 = X_1 \end{cases}, \quad (20)$$

10 where $f(t)$ is a temporal function. Correspondingly,

$$\underline{\underline{F}} = \frac{\partial \underline{x}}{\partial \underline{X}} = \begin{pmatrix} \sqrt{2f(t) + 1} & 0 \\ 0 & 1 \end{pmatrix}, \quad (21)$$

11

$$\underline{\underline{C}} = {}^t \underline{\underline{F}} \cdot \underline{\underline{F}} = \begin{pmatrix} 2f(t) + 1 & 0 \\ 0 & 1 \end{pmatrix} \quad (22)$$

12 and

$$\underline{\underline{E}} = \frac{\underline{\underline{C}} - \underline{\underline{1}}}{2} = \begin{pmatrix} f(t) & 0 \\ 0 & 0 \end{pmatrix}. \quad (23)$$

13 Because the mapping is uniform, one simply has $\underline{x} = \underline{\underline{F}} \cdot \underline{X}$. The deformed images therefore
 14 have the following intensity:

$$I_t(\underline{x}, t) = I_0(\underline{\underline{F}}^{-1} \cdot \underline{x}). \quad (24)$$

15 In practice, we generated images of size 1×1 (arbitrary units) with 100×100 pixels, $s = 0.1$
 16 (arbitrary units), 21 frames over $[0; 1]$, and $f(t) = -0.30 t$. Normal noise with zero mean
 17 and standard deviation of 0.1 (*i.e.*, signal-to-noise ratio of 10) and 0.2 (*i.e.*, signal-to-noise
 18 ratio of 5) was also added.

19 To process the synthetic images, simple square meshes with multiple element sizes were
 20 generated using GMSH⁵ [Geuzaine and Remacle, 2009].

⁵<http://gmsh.info>

1 *2.2.2. Image acquisition and combination*

2 *Image acquisition.* Standard multi-slice balanced Steady State Free Precession (SSFP) cine
 3 and whole-heart 3D Complimentary SPAtial Modulation of Magnetization (3D CSPAMM)
 4 [Rutz et al., 2008; Stoeck et al., 2012] images were acquired in a healthy volunteer (female,
 5 age 27) on a clinical 1.5T MR scanner (Philips Achieva, Best, The Netherlands). Multi-slice
 6 balanced SSFP cine images were acquired with a spatial resolution of $1.2 \times 1.2 \times 8 \text{ mm}^3$ and a
 7 temporal resolution of 35 *ms*. 3D CSPAMM images were acquired with a spatial resolution
 8 of $3.5 \times 7.7 \times 7.7 \text{ mm}^3$ reconstructed to $1 \times 1 \times 1 \text{ mm}^3$ through zero-filling in Fourier space
 9 (which corresponds to a cardinal sine interpolation in image space), a tag wave modulation
 10 period of 14 *mm* (*i.e.*, tagging distance of 7 *mm* in the magnitude images) and a temporal
 11 resolution of 28 *ms*. Image acquisition was performed during respiratory navigator gated
 12 breath-holding, and geometrical stack alignment of all tagged volume images was performed
 13 by incorporating navigator offsets and rigid image registration. More details on the imaging
 14 process can be found in [Rutz et al., 2008; Stoeck et al., 2012].

15 *Image combination.* Cine images were normalized using their maximal pixel intensity. More-
 16 over, they were resampled in order to have an isotropic pixel size, ensuring a correct inte-
 17 gration of image terms (as detailed Section 2.1.3, the quadrature of image terms is chosen
 18 such that in average there are as many integration points as pixels in each element—better
 19 quadrature should be used to correctly handle images with anisotropic pixel sizes [Pierré
 20 et al., 2016]). This processing was done using MeVisLab⁶.

21 3D CSPAMM magnetic resonance imaging produces six time series of volumetric images:
 22 magnitude and “phase” for three orthogonal tag orientations [Rutz et al., 2008; Stoeck et al.,
 23 2012]. Initial magnitude images are modulated by $|\sin(\underline{k} \underline{x})|$, where \underline{k} is the wave vector
 24 of the modulation. Thus they are not continuously differentiable, which could be an is-
 25 sue since the registration method involves image gradients. On the other hand, “phase”
 26 images simply contain the sign of the modulation, *i.e.*, $\text{sign}(\sin(\underline{k} \underline{x}))$. While in princi-
 27 ple it would be possible to reconstruct time series of continuously differentiable images
 28 ($\text{sign}(\sin(\underline{k} \underline{x})) \cdot |\sin(\underline{k} \underline{x})| = \sin(\underline{k} \underline{x})$ is indeed differentiable), in practice, however, such
 29 smooth reconstruction is not possible because of noise. Nevertheless, magnitude images
 30 are smooth enough to be used directly for the registration. Thus, the three time series of
 31 orthogonal tagged images were combined into a single time series:

$$I = \sqrt[3]{I_1 I_2 I_3}, \quad (25)$$

32 where the cube root introduces another source of theoretical non differentiability that, in
 33 practice, does not generate issues as the non differentiability is smoothed out by the image
 34 sampling. More importantly, this allows to keep a reasonable contrast in the combined
 35 images. Similar to untagged images, the combined tagged images were normalized using
 36 their maximal pixel intensity.

⁶<http://www.mevislab.de>

2.2.3. Image segmentation

The left ventricle was manually segmented on the cine and 3D CSPAMM images using MeVisLab. For cine images, the first frame was used, *i.e.*, end-diastole. For tagged images, the last frame (which is not exactly end-diastole since the last part of the cardiac cycle is not imaged [Rutz et al., 2008; Stoeck et al., 2012]) was used because of absent blood pool signal and hence better contrast between myocardium and lumen. The surface meshes generated by MeVisLab were then used to generate volume meshes using GMSH, which first reparametrizes the surface meshes, remeshes them with proper finite elements, and then generates the volume meshes [Geuzaine and Remacle, 2009; Remacle et al., 2010]. For the sake of simplicity, first order finite elements were used, though the method can be used with higher order elements in order to improve convergence. Finally, a local pseudo-prolate spheroidal coordinate system was assigned to all nodes and elements of the mesh to define local transmural, circumferential and longitudinal directions. More details on the pipeline for reconstruction of the left ventricular mesh can be found in [Genet et al., 2014, 2015].

For finite element-based image registration on untagged images, it is necessary for the mesh to extend on both sides of the object boundary if one wants to track its motion in both directions. Indeed, the correlation only happens under the mesh, so that if the boundary moves toward the outward normal (*i.e.*, away from the mesh), and if there is no contrast in the image under the mesh, then the boundary motion will not be tracked. (If the boundary moves toward the inward normal, then it will be tracked.) Thus, for cine images, a layer of elements was added around the mesh using GMSH, which has the ability to extrude surfaces in the direction of their normal [Geuzaine and Remacle, 2009]. These elements are used to enhance the image registration but not for strain analysis.

For image registration on tagged images, the registration is run backwards in time, *i.e.*, from the last to the first image in the series, since the mesh is actually created on the last image. As a consequence, strains are naturally defined from the last image, which is usually around mid-diastole [Rutz et al., 2008; Stoeck et al., 2012]. In order to express strains with respect to end-diastole, *i.e.*, the first image of the series, we need to multiplicatively combine the transformation gradients:

$$\underline{\underline{F_{0 \rightarrow t}}} = \underline{\underline{F_{T \rightarrow t}}} \cdot \underline{\underline{F_{0 \rightarrow T}}} = \underline{\underline{F_{T \rightarrow t}}} \cdot \underline{\underline{F_{T \rightarrow 0}}}^{-1}, \quad (26)$$

where $\underline{\underline{F_{0 \rightarrow t}}}$ is the gradient of the mapping from the first image 0 to the current image t , $\underline{\underline{F_{T \rightarrow t}}}$ is the gradient of the mapping from the last image T to the current image t , and $\underline{\underline{F_{0 \rightarrow T}}}$ is the gradient of the mapping from the first to the last image, *i.e.*, of the inverse mapping from the last to the first image. Note that both $\underline{\underline{F_{T \rightarrow t}}}$ and $\underline{\underline{F_{T \rightarrow 0}}}$ are computed during the registration process, so that $\underline{\underline{F_{0 \rightarrow t}}}$ can be computed explicitly from Equation (26). Then, Green-Lagrange strains with end-diastole as reference configuration can be directly computed from $\underline{\underline{F_{0 \rightarrow t}}}$.

3. Results & Discussion

3.1. Validation on *in silico* images

3.1.1. Influence of regularization strength

We first consider the simple problem of a uniformly deforming image (see Section 2.2 for details on images synthesis), and study the influence of regularization type (hyperelastic *vs.* equilibrated), as well as regularization strength β , on the computed strains. Since the images are 2D, a plane strain assumption is made in the mechanical model used in the regularization. Figure 1 shows the deforming images (for different noise and deformation levels) with superimposed warped meshes (for both hyperelastic and equilibrated warping). Regularization strength was $\beta = 0.1$ for all cases. One can see that equilibrated warping provides almost perfect registration, while hyperelastic warping results in underestimated and more noisy strains.

This is better seen in Figure 2, which shows the final computed longitudinal strain (mean \pm standard deviation over the mesh) for both methods and for the different noise levels. We consider Green-Lagrange strain, the reference configuration being the undeformed mesh, which corresponds to the initial undeformed image. Ground truth is -30% homogeneous longitudinal strain, all other components being null. In the case of hyperelastic warping, the mesh does not deform at all if the regularization strength β is close to 1, because the hyperelastic regularization basically makes the mesh extremely stiff. When the regularization strength β decreases, the computed strain tends to converge toward the exact value. For noise-free images, it does converge exactly toward ground truth. For noisy images, there is an optimum (here *ca.* $\beta = 0.1$) for which the mean strain is closest to the exact value and standard deviation is still limited; however, further reduction in the regularization strength leads to divergence of the mean and the standard deviation from ground truth. Conversely, in case of equilibrated warping, the registration is almost perfect, over a wide range of regularization strengths. For noise-free images, it is actually perfect for all regularization strengths. For noisy images, as long as there is enough regularization (here *ca.* $\beta > 0.001$) to get the registration to converge, the registration is almost perfect.

Similar conclusions can be drawn from Figure 3, which shows the normalized image similarity root mean square error (RMSE) at the last time frame T , *i.e.*

$$\text{RMSE} = \frac{\sqrt{\Psi^{\text{im}}}}{\sqrt{\int_{\Omega_0} I_0^2 d\Omega_0}} = \frac{\sqrt{\int_{\Omega_0} (I_T \circ \underline{\varphi} - I_0)^2 d\Omega_0}}{\sqrt{\int_{\Omega_0} I_0^2 d\Omega_0}}, \quad (27)$$

as a function of regularization strength β . For large values of regularization strength, hyperelastic warping heavily degrades the registration, and the image similarity error is largely above the noise level. When decreasing the regularization strength, the image similarity error converges toward noise level. (The convergence is slower for noise-free images, simply because for noisy images the error is noise-dominated for $\beta < 0.1$.) Conversely, with

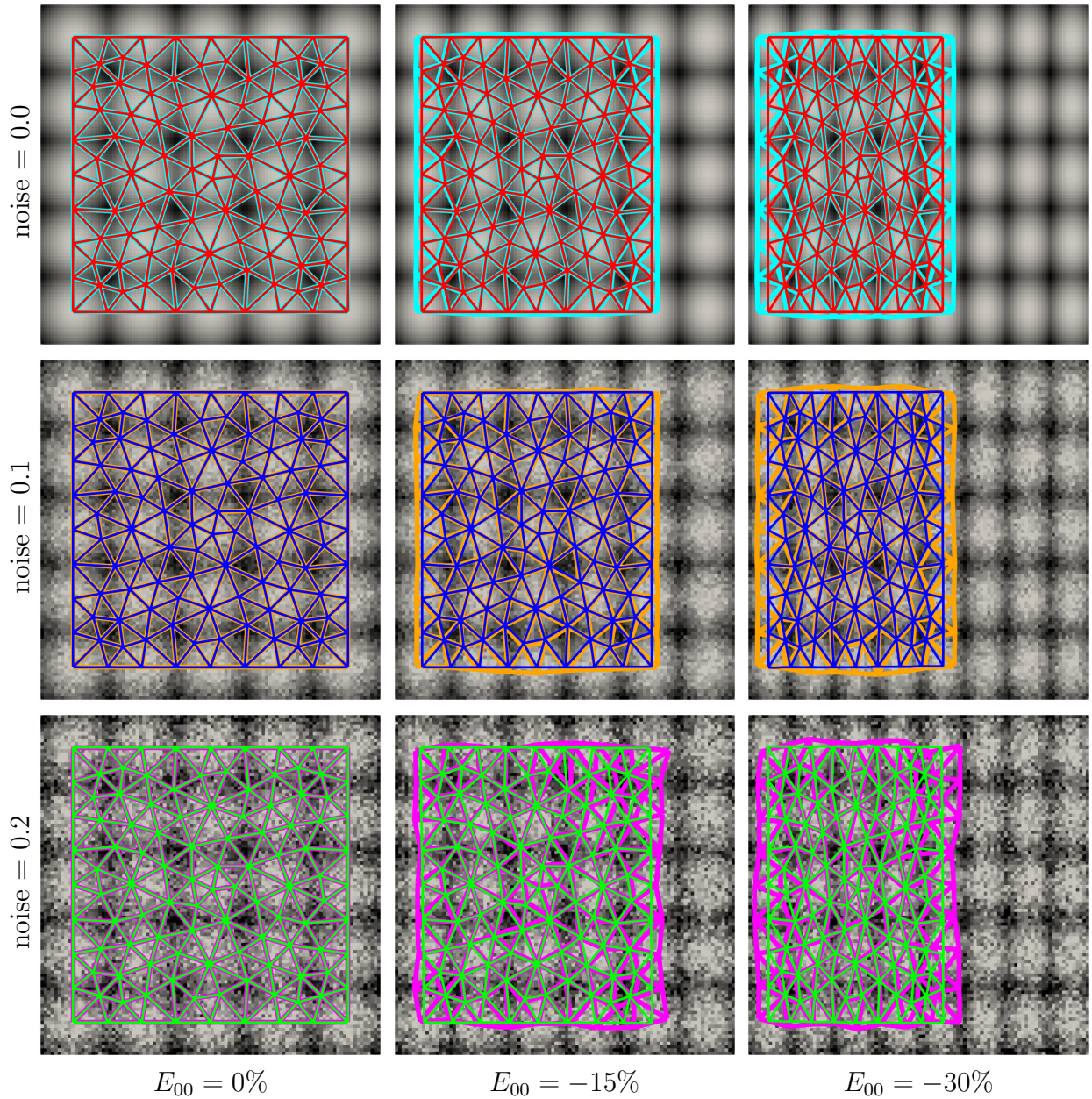


Figure 1: Results on synthetic data. Uniformly deformed images (exact strain is thus homogeneous) with superimposed meshes obtained with equilibrated and hyperelastic warping. Each row shows a different noise level (0.0, 0.1 & 0.2), while each column shows a different deformation level (0%, -15% & -30%). Results for equilibrated warping are shown in red, blue & green, while results for hyperelastic warping are shown in cyan, orange & magenta. Regularization strength was $\beta = 0.1$ for all cases. One can see that equilibrated warping provides almost perfect registration, while hyperelastic warping provides underestimated and more noisy strains.

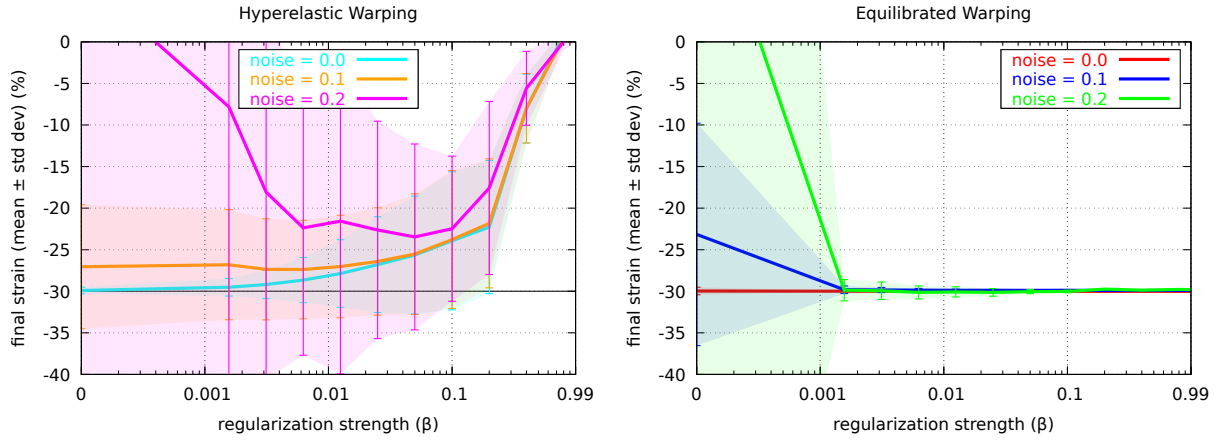


Figure 2: Results on synthetic data. Final measured longitudinal Green-Lagrange strain (mean \pm standard deviation over the mesh) as a function of regularization strength β , for hyperelastic (left) and equilibrated (right) warping, and for different noise levels (0.0, 0.1 & 0.2). Ground truth is -30% homogeneous strain. Hyperelastic regularization has a very strong impact on registration, and is very sensitive to regularization strength. Conversely, equilibrium gap regularization has a much reduced impact on registration.

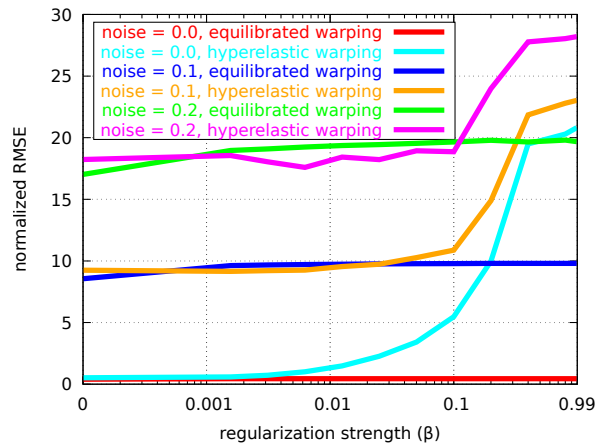


Figure 3: Results on synthetic data. Final normalized image similarity error as a function of regularization strength β , for equilibrated and hyperelastic warping, and for different noise levels. Again, hyperelastic regularization has a very strong impact on registration, contrary to equilibrium gap regularization.

1 equilibrated warping, the image similarity error is close to noise level independently of the
2 regularization strength. It is interesting to see that for small values of regularization strength,
3 the image similarity error is close to noise level even though the actual strain is far from
4 ground truth, meaning that image similarity error is not a good criterion for the success of
5 the registration.

6 This result illustrates a general weakness of the hyperelastic regularization, and the
7 main strength of the equilibrium gap regularization. Indeed, the exact uniform strain is
8 not a minimizer of the hyperelastic energy, but it is a minimizer of the equilibrium gap
9 energy. Actually the unique minimizer of the hyperelastic energy is the null deformation,
10 so that strain measurements are always compromised. Conversely, any deformation that
11 corresponds to the solution of a hyperelastic body in equilibrium with surface loads is a
12 minimizer of the equilibrium gap energy, so that it minimally affects strain measurements.

13 3.1.2. Influence of mesh density

14 We now study the influence of mesh density on the registration. The mesh used in the
15 previous section was successively refined until the elements reached the image pixel size.
16 They are shown in the left column of Figure 4, while the middle and right column show the
17 registration results (final strain as a function of regularization strength, similar to Figure 2)
18 for hyperelastic and equilibrated warping, respectively.

19 When the mesh is refined, the signal-to-noise ratio on each finite element decreases, and
20 larger regularization strengths are required to perform the registration and obtain satisfy-
21 ing strains. As a result, the range of registration strengths that provide satisfying strains
22 becomes smaller. This is the case for both regularization methods; however, this is more crit-
23 ical for hyperelastic regularization, for which the range of acceptable regularization strengths
24 becomes very narrow. Conversely, for equilibrium gap regularization, the impact of mesh
25 size is less critical.

26
27 Further validation of the proposed method based on the Cardiac Motion Tracking Chal-
28 lenge [Tobon-Gomez et al., 2013] is provided in Appendix A.

29 3.2. Results on *in vivo* images

30 We now consider *in vivo* tagged and untagged cardiac MR images of a healthy human
31 subject (see Section 2.2 for details on image acquisition, combination and segmentation).

32 3.2.1. Results on *in vivo* tagged images

33 *Finding the optimal regularization strength.* Similarly to Figure 2 for synthetic images, Fig-
34 ure 5 shows the influence of regularization strength β on strain extracted from tagged im-
35 ages using equilibrated warping. Here we consider Green-Lagrange strains at end-systole
36 with regard to end-diastole, rotated in local pseudo-prolate spheroidal coordinates (trans-
37 mural, circumferential, longitudinal), and we show the mean \pm standard deviation across
38 the entire ventricle. For circumferential and longitudinal components, as well as for the
39 circumferential-longitudinal shear component (*i.e.*, the out-of-plane twist), the trend is sim-
40 ilar to that found with the *in silico* images: above a given regularization strength (here *ca.*

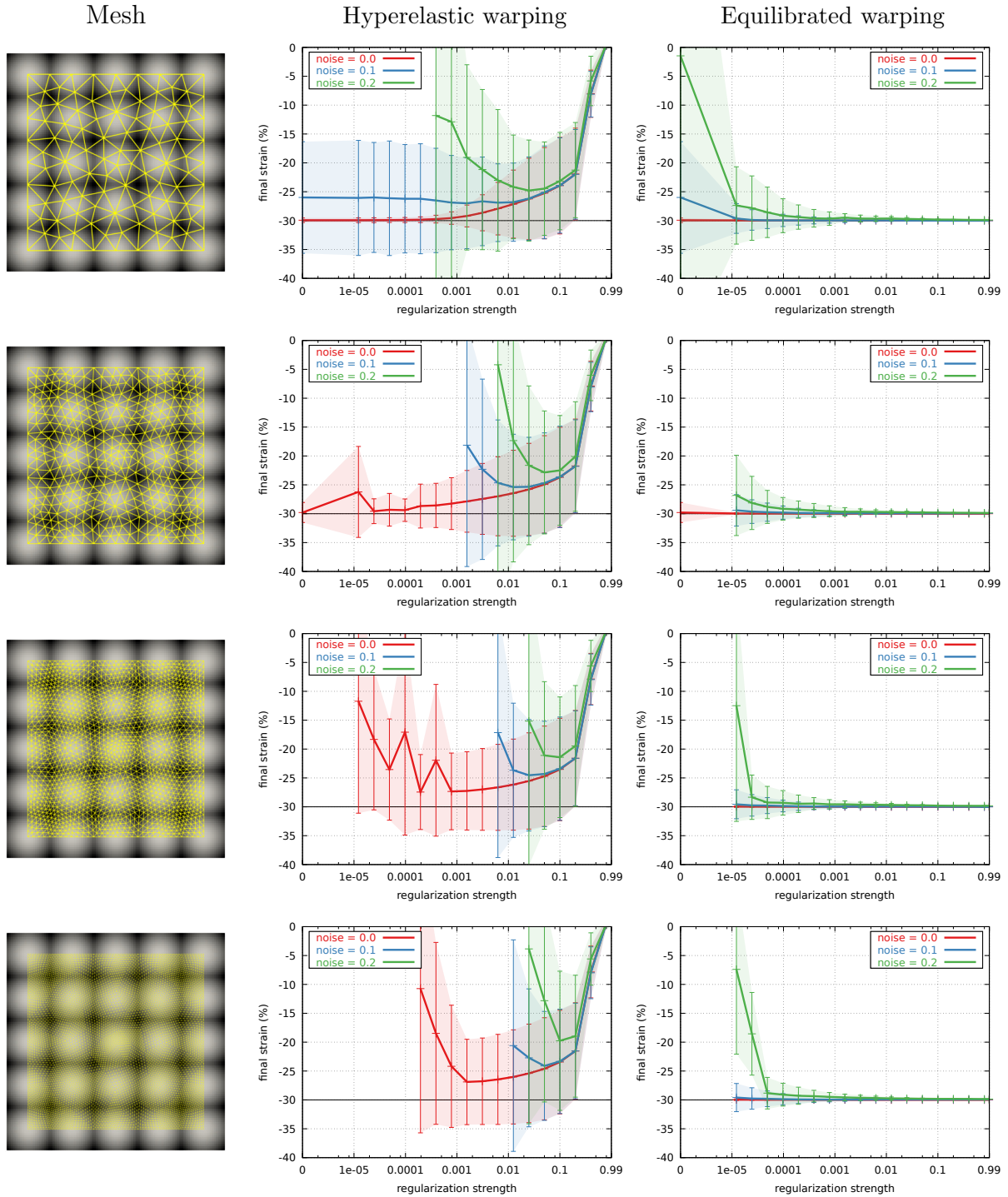


Figure 4: Results on synthetic data. Each line corresponds to a mesh refinement level. Left column shows the mesh, while middle and right columns show registration results (final strain as a function of regularization strength, similar to Figure 2) for hyperelastic and equilibrated warping, respectively. Failed computations (because of divergence or large unrealistic strains) have been removed. For both regularization methods, stronger regularization is required for finer meshes. However, the impact of mesh size is more benign for equilibrated warping compared to hyperelastic warping.

1 $\beta = 0.1$) the equilibrium gap regularization does not significantly affect the mean computed
2 strains, though increasing the regularization strength does reduce their standard deviation.
3 Conversely, radial strain is not very well captured and is largely underestimated—decreasing
4 regularization strength does increase mean radial strain toward more realistic values, but at
5 the cost of a very large standard deviation.

6 *Strain measurement.* Figure 6 shows the results of the registration (for $\beta = 0.1$), with 3D
7 CSPAMM images superimposed with the deformed mesh. The motion of the left ventricle
8 is very well tracked. Figure 7 shows the temporal variations of each strain component aver-
9 aged over the entire ventricle. Figure 8 shows the spatial variations of each strain component
10 at end-systole, averaged over multiple sectors. Once again, we see that circumferential &
11 longitudinal shortenings are very well captured, as well as circumferential-longitudinal (*i.e.*,
12 out-of-plane) twist. Moreover, these components are mostly homogeneous within the ventri-
13 cle, as expected for a healthy heart [Moore et al., 2000]. Furthermore, longitudinal variation
14 of radial-circumferential (*i.e.*, in-plane) twist, with positive rotation differential between en-
15 docardium and epicardium at apex and negative rotation differential at base [Bertini et al.,
16 2010], was correctly captured. Conversely, radial thickening is largely underestimated. This
17 has already been noted in [Tobon-Gomez et al., 2013], using other registration methods.
18 It is due to the limited spatial resolution of $3.5 \times 7.7 \times 7.7 \text{ mm}^3$, which leads to partial
19 voluming at the endo- and epicardial surfaces and thus reduced accuracy of in-plane motion
20 tracking. We are currently working on characterizing the impact of image resolution on
21 measured radial strains.

22 3.2.2. Results on in vivo untagged images

23 *Finding the optimal regularization strength.* We now show similar results for untagged im-
24 ages. Figure 9 is analogous to Figure 5, and shows end-systolic strain as a function of
25 regularization strength. Impact of equilibrium gap regularization on average circumferential
26 & longitudinal strains is again limited, albeit slightly larger than for tagged images, and
27 without clear convergence of the mean value in the radial strain. Moreover, except for very
28 large regularization strength, there is a spurious radial-longitudinal deformation, which is
29 located toward the free wall of the ventricle. This is due to the fact that, besides lack of
30 texture, short-axis cine stacks have very poor longitudinal resolution, so that tracking of
31 the myocardium, especially toward the base, is not robust. We are currently working on
32 combining both short-axis and long-axis cine images in order to overcome this difficulty.

33 *Strain measurement.* Figures 10, 11 & 12 show, for $\beta = 0.1$, cine images superimposed with
34 the deformed mesh, temporal and spatial variations of strains, respectively. As opposed to
35 that found in the tagged images, radial thickening is very well captured by the equilibrated
36 warping method. The method was even able to capture regional variations of radial strain:
37 it is larger in the left ventricular free wall than in the septum [Moore et al., 2000], as a
38 consequence of being pressurized on both side. Circumferential and longitudinal shortenings
39 are also well captured. Despite the spurious radial-longitudinal strain, it is interesting
40 that the method was able to capture some in-plane (*i.e.*, radial-circumferential) and out-of-
41 plane (*i.e.*, circumferential-longitudinal) twists, even though there is no contrast within the

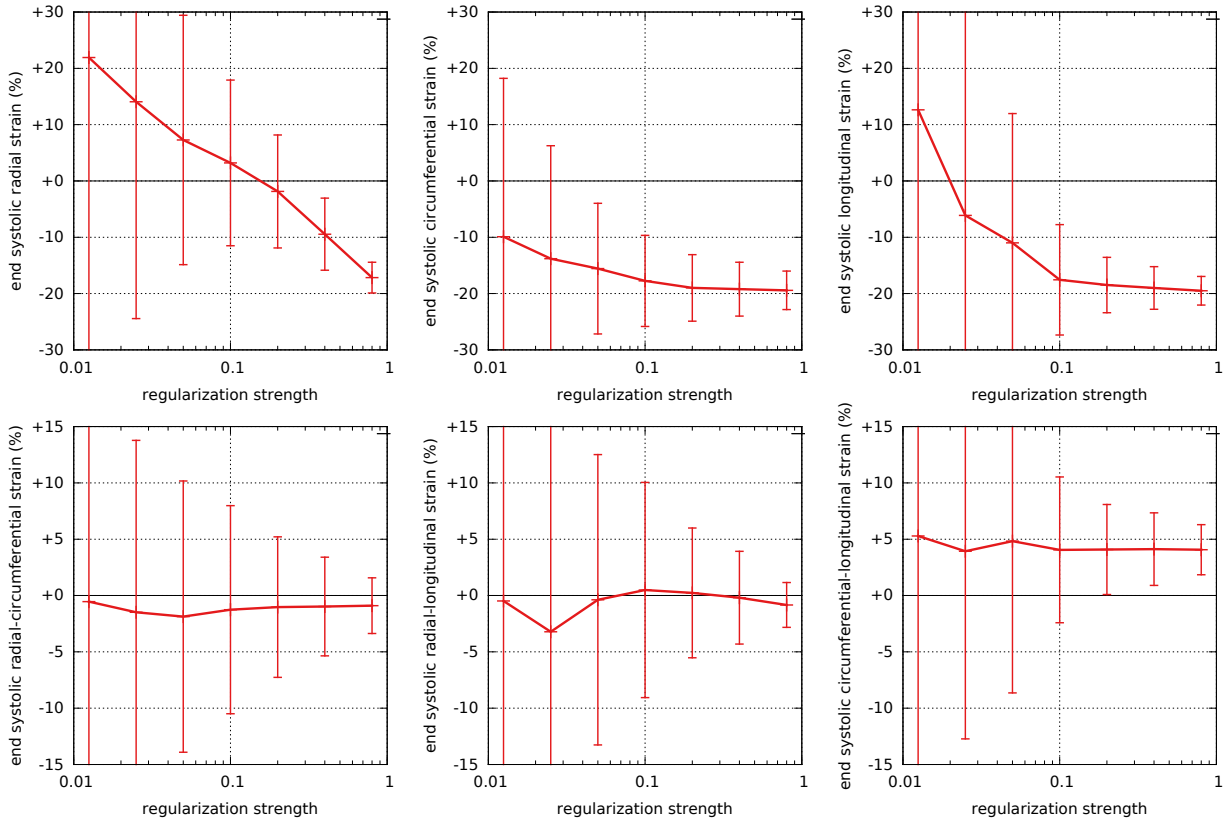


Figure 5: Results on *in vivo* tagged data. Green-Lagrange strain components at end-systole with respect to end-diastole (mean \pm standard deviation over the ventricle) as a function of regularization strength. Except for radial strain (top left), for all other components, including circumferential (top center), longitudinal (top right) and circumferential-longitudinal (bottom right) components, the equilibrium gap regularization has a limited impact on the registration above a certain level of regularization required to regularize the registration problem.

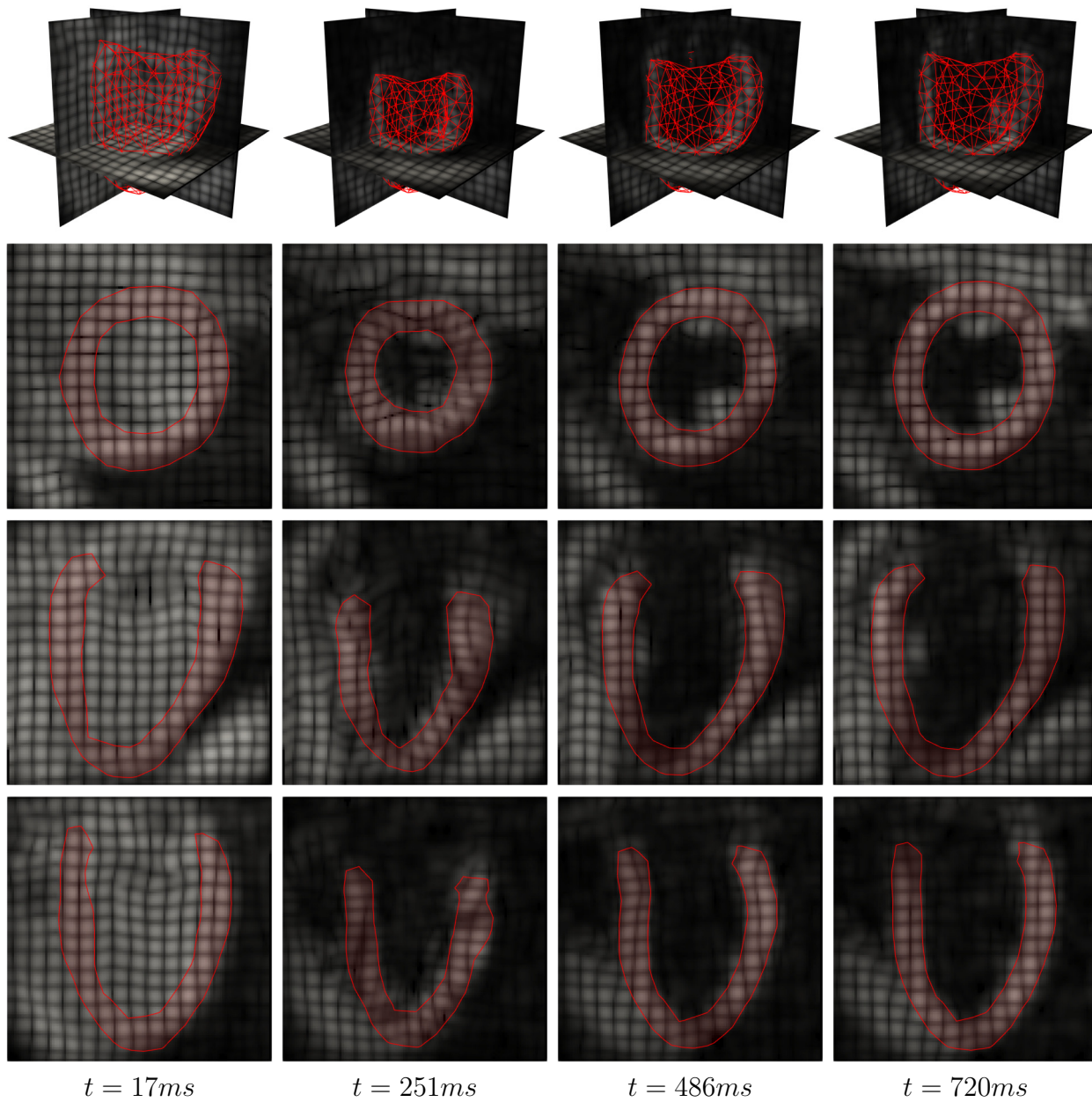


Figure 6: Results on *in vivo* tagged data. Sequence of 3D CSPAMM images with superimposed warped mesh, for a regularization strength of $\beta = 0.1$. First row shows 3D view, while second, third and fourth rows show short axis, two-chamber and four-chamber views, respectively.

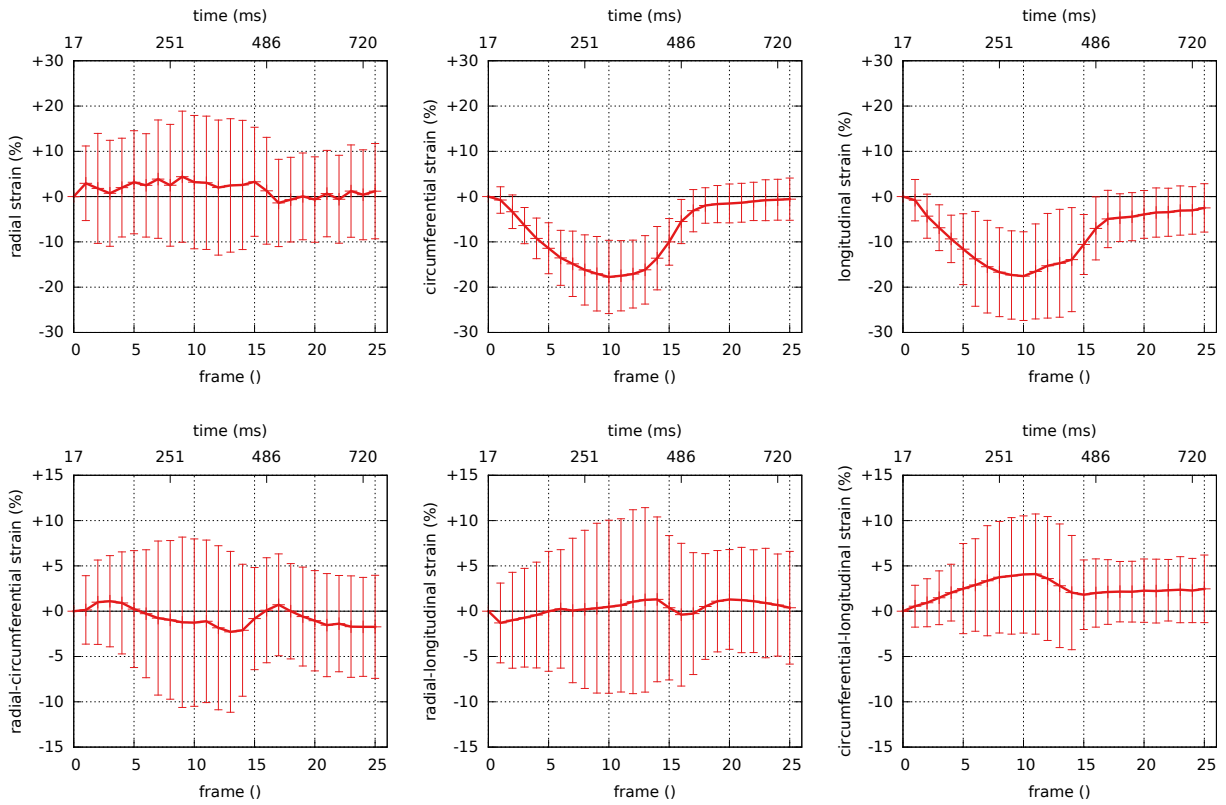


Figure 7: Results on *in vivo* tagged data. Green-Lagrange strain components with respect to end-diastole (mean \pm standard deviation over the ventricle) as a function of time, for a regularization strength of $\beta = 0.1$. Circumferential & longitudinal shortenings, as well as circumferential-longitudinal (*i.e.*, out-of-plane) twist are well captured. Conversely, radial thickening is largely underestimated.

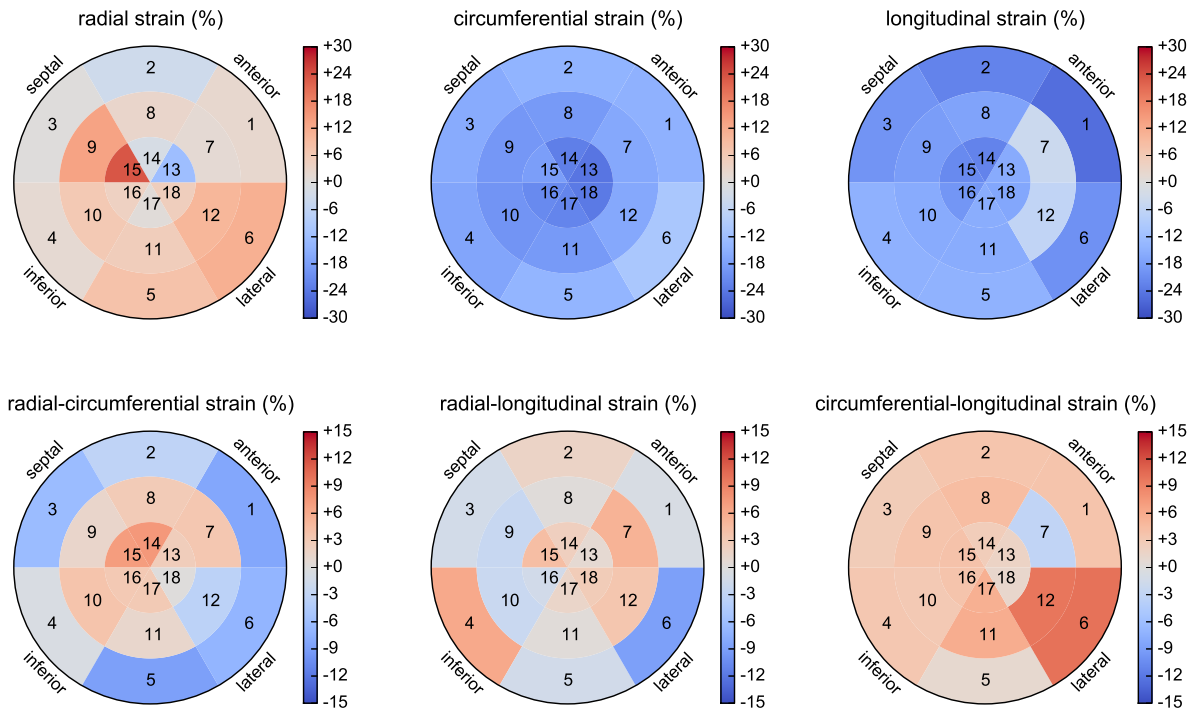


Figure 8: Results on *in vivo* tagged data. Bull's eye plots of end-systolic Green-Lagrange strains, for a regularization strength of $\beta = 0.1$. The left ventricle was split into 18 sectors (6 circumferential and 3 longitudinal sections, see Figure 12), and strains were averaged over each sector. Numbers within sectors represent their ID, as described on Figure 12. Circumferential, longitudinal and circumferential-longitudinal components are mostly homogeneous within the ventricle, which is expected for a normal case [Moore et al., 2000]. Longitudinal variation of radial-circumferential shear is captured as well [Bertini et al., 2010].

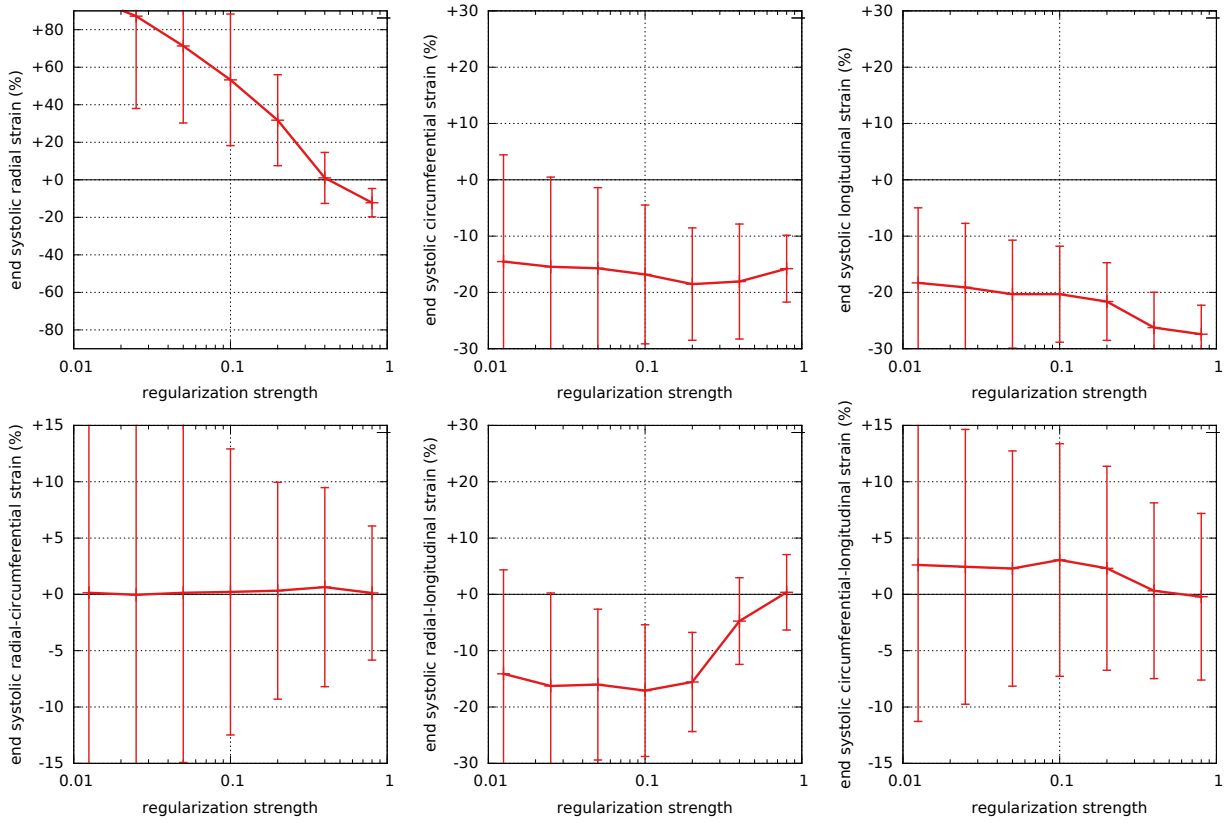


Figure 9: Results on *in vivo* untaged data. Green-Lagrange strain components at end-systole with respect to end-diastole (mean \pm standard deviation over the ventricle) as a function of regularization strength. As for tagged images, the equilibrium gap regularization has a limited impact on the registration.

1 myocardial wall in the untagged images. This is induced by the motion of the neighboring
2 features to the myocardium such as papillary muscles and pericardial fluid, which are present
3 in the boundary layer of elements used to improve tracking of endocardium & epicardium
4 (see Section 2.2.3 for details). Indeed, tracking without boundary layer (not shown here)
5 shows much reduced radial thickening, and almost no twist at all. Nevertheless, this is not a
6 local measurement *per se*. We will further investigate the ability to measure heterogeneous
7 strain fields, in case of myocardial infarction for instance.

8 3.3. Limitations

9 The proposed method has a number of limitations that we want to emphasize here.
10 First of all, the finite element approach to image registration requires a segmentation and
11 a mesh for the processing, which can be a drawback compared to other methods that work
12 directly on the images. However, having a finite element mesh as support of the sought after
13 displacement fields allows to define consistent functional spaces, with specific smoothness
14 properties; moreover it opens the door for the combined processing of multiple images with
15 different orientations and discretizations.

16 This points to another limitation of the current implementation of the method, where
17 only one image set can be used at a time. Consequently, short-axis cine stacks need to be
18 interpolated in the longitudinal direction, leading to registration errors as seen on Figure 10.
19 Combining short-axis cine stacks and long-axis cine slices, and even untagged and tagged
20 images, will probably improve registration significantly.

21 Specifically to the regularization method introduced here, even though equilibrium gap
22 regularization was designed to have a limited bias on the strain results, it might still have a
23 non-negligible impact on strains. Indeed, any mapping that is the solution of a hyperelastic
24 body in equilibrium with surface loads is the minimizer of $\Psi^{\text{reg, equil}}$, so that the actual solution
25 is probably close to a minimizer—this must be compared to hyperelastic regularization,
26 where only the null mapping is a minimizer of the $\Psi^{\text{reg, hyper}}$, hence the large bias on strain
27 results. However, because of anisotropy, contraction, and possibly non-affine deformation
28 patterns, the actual solution might still be far from the equilibrium solution of the isotropic
29 hyperelastic model postulated here, which could explain the poor tracking of radial strain
30 found in Figure 7. It could also explain the fact that radial strains do not converge toward
31 a given value when decreasing regularization strength, but keep increasing, on both tagged
32 and untagged images, as seen in Figures 5 & 9. More complex behavior laws could be used
33 to address this issue.

34 4. Conclusion

35 Equilibrated warping is a powerful method for non-rigid registration of images involving
36 arbitrary large deformation. The equilibrium gap constraint regularizes the image regis-
37 tration problem, even in presence of noise, with limited effect on strain measurement, as
38 demonstrated using synthetic data. The method has been implemented based on FEniCS
39 and VTK, providing an efficient tool for 2D & 3D images registration. When applied to
40 cardiac MR images, it allows to extract the main features of left ventricular deformation.

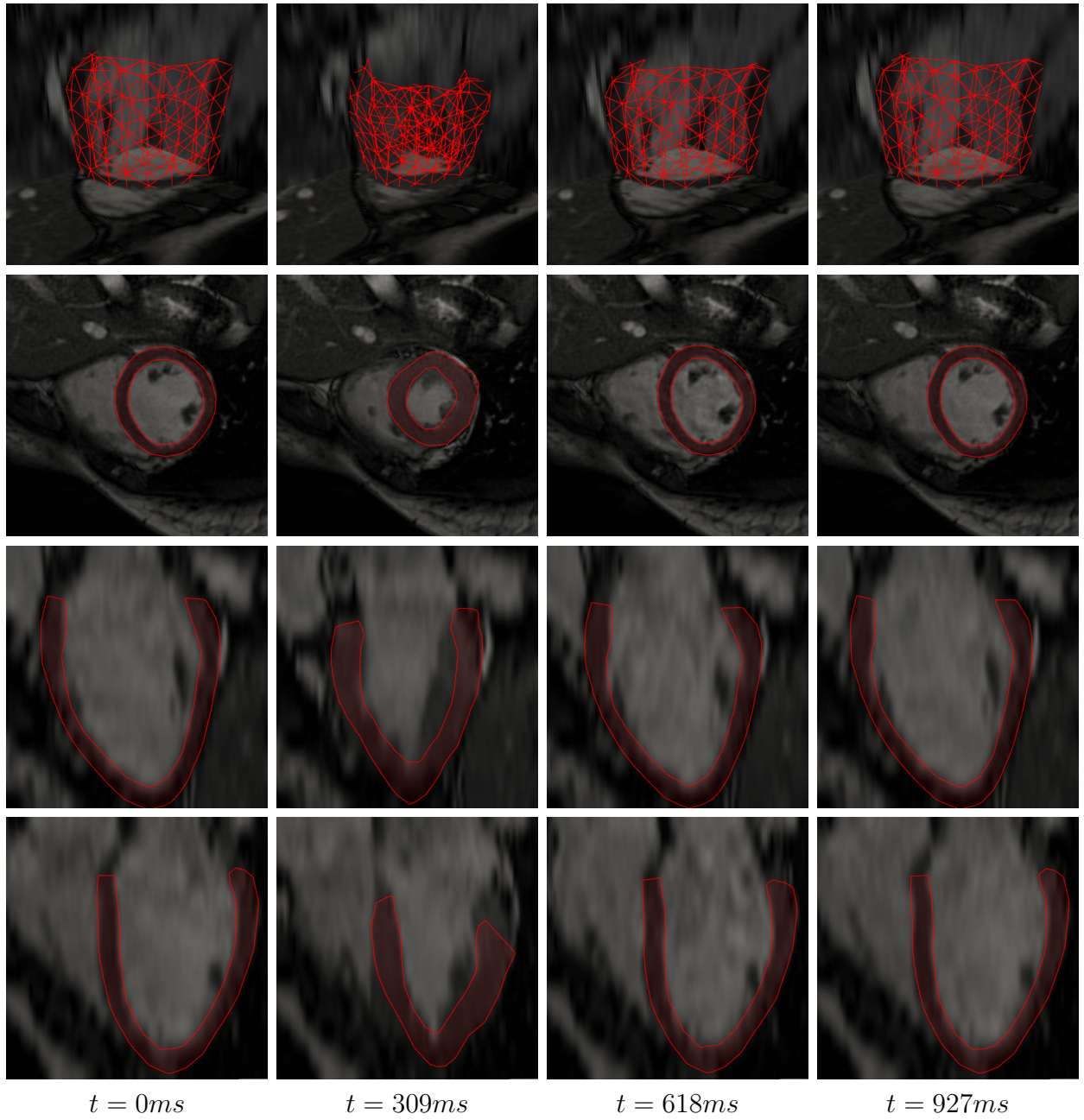


Figure 10: Results on *in vivo* untagged data. First row shows 3D view, while second, third and fourth rows show short axis, two-chamber and four-chamber views, respectively.

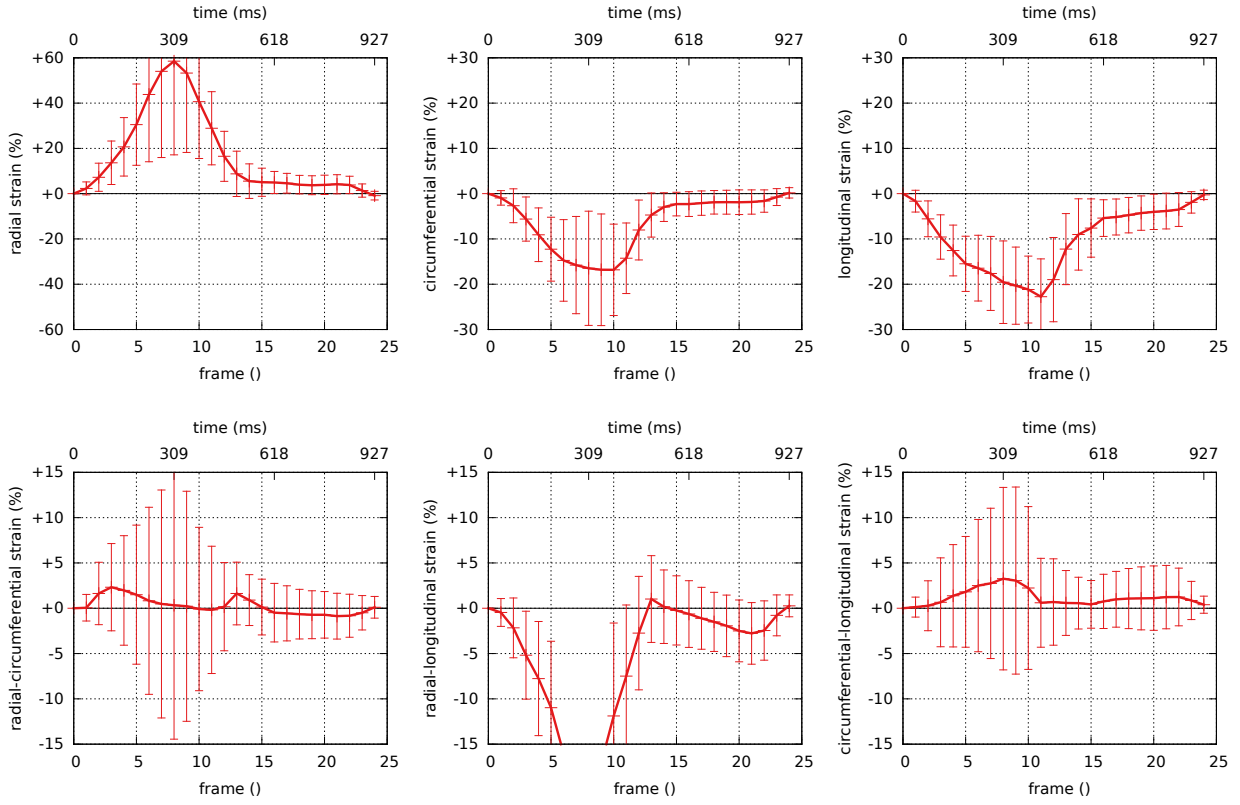


Figure 11: Results on *in vivo* untaged data. Green-Lagrange strain components with respect to end-diastole (mean \pm standard deviation over the ventricle) as a function of time, for a regularization strength of $\beta = 0.1$. Despite a spurious radial-longitudinal motion, the method was able to capture circumferential and longitudinal shortenings, but also radial thickening as well as in-plane (*i.e.*, radial-circumferential) and out-of-plane (*i.e.*, circumferential-longitudinal) twists.

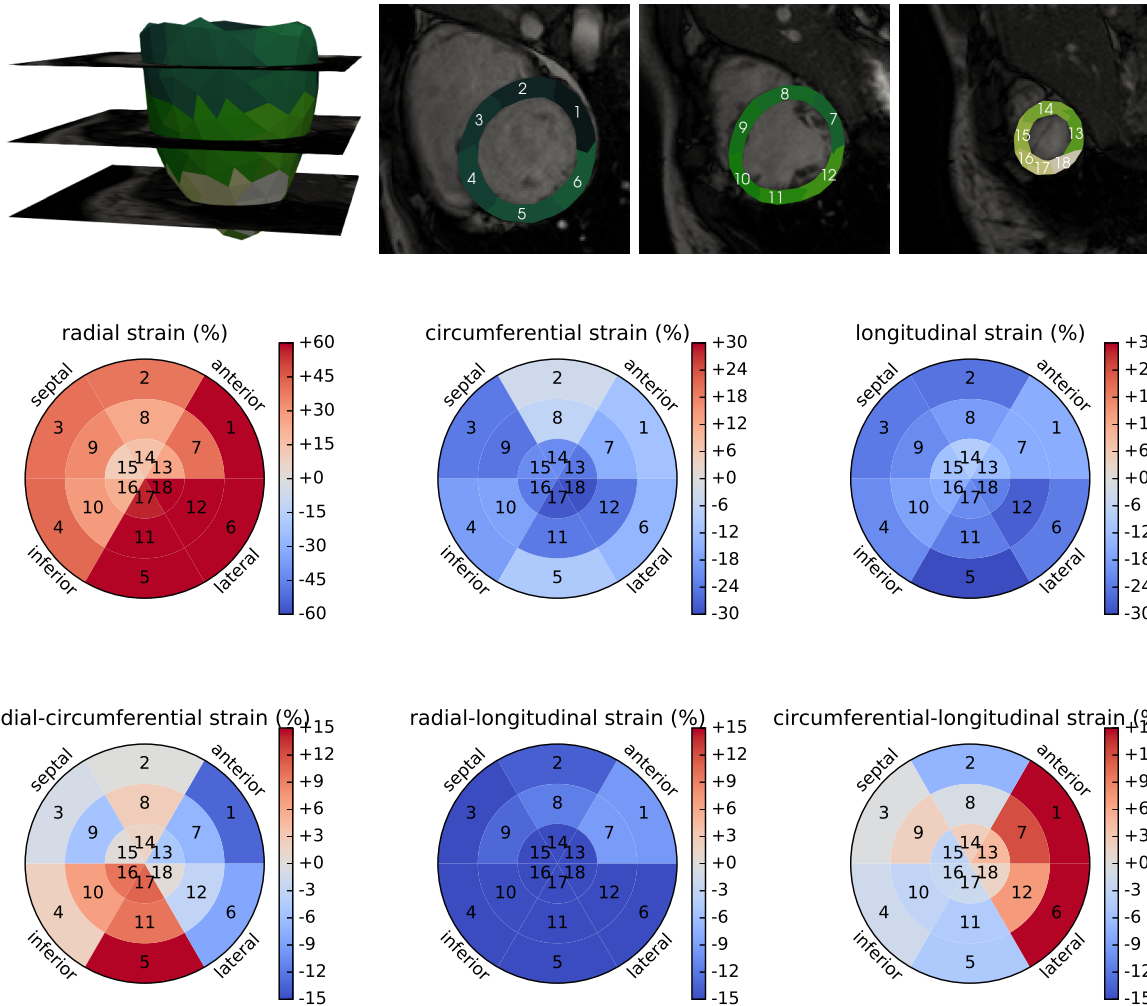


Figure 12: Results on *in vivo* untaged data. Top row: Left ventricular mesh split into 18 sectors (6 circumferential and 3 longitudinal sections). Bottom rows: Bull's eye plots of end-systolic Green-Lagrange strains, for a regularization strength of $\beta = 0.1$. Numbers within sectors represent their ID, as described on the top row. Strains are generally more heterogeneous than for tagged images. However, it is interesting to note that radial strains are more important in the free wall than in the septum, which is expected since the septum is pressurized on both sides.

Appendix A. Validation using Motion Tracking Challenge

In order to further validate the proposed image registration framework, we processed the public dataset of the Cardiac Motion Analysis Challenge that was held at the 2011 MICCAI workshop⁷, and is described in details in [Tobon-Gomez et al., 2013]. Briefly, the dataset consists of untagged (SSFP) and tagged (3DTAG) images (3DUS images were not processed), segmentations and markers that were manually tracked by experts on the images (*i.e.*, ground truth, GT), for a dynamic phantom (PHANTOM) and fifteen healthy volunteers (V1, V2, V4-V16). Results, in terms of tracked markers, from the challenge competitors (INRIA, IUCL, MEVIS, UPF) are also provided.

We first generated volume meshes from the segmented surfaces using GMSH, as described in Section 2.2.2. (Segmented surface V8 was slightly distorted toward the base and could not be meshed, so this dataset was not analyzed.) Then, we run the equilibrated warping method on each dataset, with various regularization strengths, and interpolated the obtained displacement fields onto the markers. In order to assess the quality of the registration, the following normalized error on the markers trajectory was used:

$$\text{err} = \frac{1}{n_{\text{markers}}} \sum_{m=1}^{n_{\text{markers}}} \frac{\sum_{f=1}^{n_{\text{frames}}} \|\underline{X}^m(f) - \underline{X}^{m,\text{GT}}(f)\|}{\sum_{f=1}^{n_{\text{frames}}-1} \|\underline{X}^{m,\text{GT}}(f+1) - \underline{X}^{m,\text{GT}}(f)\|}, \quad (\text{A.1})$$

where n_{markers} is the number of “valid” markers (*i.e.*, markers that lie within the mesh in the reference configuration and can thus be tracked), n_{frames} is the number of frames, $\underline{X}^{m,\text{GT}}(f)$ is the ground truth position of marker m at frame f , and $\underline{X}^m(f)$ is the tracked position of marker m at frame f . In Figure A.1, we show this normalized markers error as a function of regularization strength, for the PHANTOM as well as the fourteen processed volunteers (V1, V2, V4-V7, V9-V16), for both 3DTAG and SSFP images. We also completed the normalized markers error for the results of the challenge competitors, which are shown on the plots. One can see that the regularization strength has a limited impact on registration. Moreover, the registration is overall quite satisfactory, with a normalized markers error always in the range of the other established methods. (With the exception of V11–SSFP results for $\beta = 0.1$, for which the tracking failed.)

Figure A.2 shows the normalized markers error for all cases, for both 3DTAG and SSFP images, for all competitors as well as the proposed method for $\beta = 0.1$ and best β (which varies from one case to the other), in a bar plot. We also showed the average and standard deviation of normalized markers error over all cases (rightmost columns of the plot). This shows that the proposed method compares well to the other established methods.

Appendix B. Vitae

Appendix B.1. Martin Genet

Martin Genet obtained his PhD from *École Normale Supérieure*, Cachan, France, in 2010, and was then a postdoctoral fellow at the Lawrence Berkeley National Laboratory,

⁷<http://www.cardiacatlas.org/challenges/motion-tracking-challenge>

1 California, USA, from 2010 to 2012. In 2012 he obtained a Marie-Curie International Out-
2 going fellowship to work on patient-specific cardiac modeling, at the University of California
3 at San Francisco, USA, and Stanford University, Palo Alto, USA, from 2012 to 2014, and at
4 the Swiss Federal Institute of Technology (ETH), Zurich, Switzerland, from 2014 to 2015.
5 Since 2015 he is an Assistant Professor at *École Polytechnique*, Palaiseau, France, where he
6 works on mechanical modeling and simulation, with data interaction, of soft tissues.

7 *Appendix B.2. Christian Stoeck*

8 Christian T. Stoeck obtained his PhD from ETH Zurich in Switzerland in 2014. He
9 then worked as postdoctoral scholar at King’s College London, UK, in 2014-2015 and at
10 University of Zurich, Switzerland, in 2015-2017. The research of Christian Stoeck focuses
11 on the development of novel cardiovascular imaging methodology for mechanical as well as
12 microstructural imaging of the heart and its translation into pre-clinical as well as clinical
13 environments.

14 *Appendix B.3. Constantin von Deuster*

15 Constantin von Deuster obtained his PhD in 2016 from King’s College London, UK. He
16 was working in a joint collaboration with the Division of Imaging Sciences and Biomedical
17 Engineering at King’s College London and the Institute for Biomedical Engineering at Uni-
18 versity and ETH Zurich, Switzerland. The focus of his thesis was on improving reliability of
19 magnetic resonance diffusion imaging in the in vivo human heart. Since 2016 he is a post-
20 doctoral fellow at the Institute for Biomedical Engineering at University and ETH Zurich,
21 Switzerland, continuing his work on magnetic resonance diffusion imaging, including pulse
22 sequence design and patient studies.

23 *Appendix B.4. Lik Chuan Lee*

24 Lik Chuan Lee is an Assistant Professor in the Department of Mechanical Engineering
25 at Michigan State University. He received his PhD in Mechanical Engineering from the
26 University of California, Berkeley, in 2010. He then worked as a postdoctoral scholar in
27 the Department of Surgery at the University of California, San Francisco, between 2010
28 and 2014 prior to joining Michigan State University. Lik Chuan Lee’s research interest
29 is in computational mechanics and his current research focus is in computational cardiac
30 modeling.

31 *Appendix B.5. Sebastian Kozerke*

32 Sebastian Kozerke, is a Professor of Biomedical Imaging at the Institute for Biomedical
33 Engineering of the University and ETH Zurich, Switzerland, where he leads the Cardiovas-
34 cular Magnetic Resonance research. He obtained his PhD degree and the *Venia legendi* from
35 ETH Zurich in 2000 and 2005, respectively. In 2002-03 he was a research associate at the
36 Division of Imaging Sciences at King’s College London, UK. He was elected as a Professor
37 and Chair of MR physics at King’s College London in 2008 before being promoted to Pro-
38 fessor at the University of Zurich in 2010. In 2014 he was elected as full Professor at ETH
39 Zurich. The research of Sebastian Kozerke spans from developments in MR pulse sequence

1 design, scan acceleration techniques, novel information encoding concepts, dynamic nuclear
2 polarization techniques to experimental validation and clinical translation of MR methods.

3 References

- 4 Alnæs, M., Blechta, J., Hake, J., Johansson, A., Kehlet, B., Logg, A., Richardson, C., Ring, J., Rognes,
5 M. E., Wells, G. N., 2015. The FEniCS Project Version 1.5. Tech. rep., University Library Heidelberg.
- 6 Arts, T., Prinzen, F. W., Delhaas, T., Milles, J. R., Rossi, A. C., Clarysse, P., 2010. Mapping displacement
7 and deformation of the heart with local sine-wave modeling. *IEEE Transactions on Medical Imaging*
8 29 (5), 1114–23.
- 9 Axel, L., Dougherty, L., 1989. MR imaging of motion with spatial modulation of magnetization. *Radiology*
10 171, 841–845.
- 11 Bertini, M., Delgado, V., Nucifora, G., Ajmone Marsan, N., Ng, A. C. T., Shanks, M., Antoni, M. L.,
12 van de Veire, N. R. L., van Bommel, R. J., Rapezzi, C., Schalij, M. J., Bax, J. J., Nov. 2010. Left
13 ventricular rotational mechanics in patients with coronary artery disease: Differences in subendocardial
14 and subepicardial layers. *Heart* 96 (21), 1737–1743.
- 15 Burger, M., Modersitzki, J., Ruthotto, L., Jan. 2013. A Hyperelastic Regularization Energy for Image
16 Registration. *SIAM Journal on Scientific Computing* 35 (1), B132–B148.
- 17 Chappelle, D., Fragu, M., Mallet, V., Moireau, P., 2013. Fundamental principles of data assimilation under-
18 lying the Verdandi library: Applications to biophysical model personalization within euHeart. *Medical*
19 *and Biological Engineering and Computing* 51, 1221–1233.
- 20 Christensen, G. E., Rabbitt, R. D., Miller, M. I., Jan. 1996. Deformable templates using large deformation
21 kinematics. *IEEE transactions on image processing : a publication of the IEEE Signal Processing Society*
22 5 (10), 1435–47.
- 23 Ciarlet, P. G., Geymonat, G., 1982. Sur les lois de comportement en élasticité non-linéaire compressible.
24 *Comptes Rendus de l’Académie des Sciences Série II* 295, 423–426.
- 25 Claire, D., Hild, F., Roux, S., 2004. A finite element formulation to identify damage fields: The equilibrium
26 gap method. *International Journal for Numerical Methods in Engineering* 61 (2), 189–208.
- 27 Delingette, H., Billet, F., Wong, K. C. L., Sermesant, M., Rhode, K., Ginks, M., Rinaldi, C. A., Razavi,
28 R., Ayache, N., Jan. 2012. Personalization of Cardiac Motion and Contractility From Images Using
29 Variational Data Assimilation. *IEEE Transactions on Biomedical Engineering* 59 (1), 20–24.
- 30 Fischer, S. E., McKinnon, G. C., Maier, S. E., Boesiger, P., Aug. 1993. Improved myocardial tagging
31 contrast. *Magnetic Resonance in Medicine* 30 (2), 191–200.
- 32 Garot, J., Bluemke, D. A., Osman, N. F., Rochitte, C. E., McVeigh, E. R., Zerhouni, E. A., Prince, J. L.,
33 Lima, J. A. C., Mar. 2000. Fast Determination of Regional Myocardial Strain Fields From Tagged Cardiac
34 Images Using Harmonic Phase MRI. *Circulation* 101 (9), 981–988.
- 35 Genet, M., Lee, L. C., Ge, L., Acevedo-Bolton, G., Jeung, N., Martin, A. J., Cambronero, N., Boyle, A. J.,
36 Yeghiazarians, Y., Kozerke, S., Guccione, J. M., Aug. 2015. A Novel Method for Quantifying Smooth
37 Regional Variations in Myocardial Contractility Within an Infarcted Human Left Ventricle Based on
38 Delay-Enhanced Magnetic Resonance Imaging. *Journal of Biomechanical Engineering* 137 (8).
- 39 Genet, M., Lee, L. C., Nguyen, R., Haraldsson, H., Acevedo-Bolton, G., Zhang, Z., Ge, L., Ordovas, K.,
40 Kozerke, S., Guccione, J. M., 2014. Distribution of normal human left ventricular myofiber stress at end
41 diastole and end systole: A target for in silico design of heart failure treatments. *Journal of Applied*
42 *Physiology* 117, 142–52.
- 43 Genet, M., Stoeck, C. T., von Deuster, C., Lee, L. C., Guccione, J. M., Kozerke, S., 2016. Finite Element
44 Digital Image Correlation for Cardiac Strain Analysis from 3D Whole-Heart Tagging. In: 24th Annual
45 Meeting of the International Society for Magnetic Resonance in Medicine (ISMRM2016).
- 46 Geuzaine, C., Remacle, J.-F., Sep. 2009. Gmsh: A three-dimensional finite element mesh generator with
47 built-in pre- and post-processing facilities. *International Journal for Numerical Methods in Engineering*
48 79 (11), 1309–1331.

- 1 Hild, F., Bouterf, A., Chamoin, L., Leclerc, H., Mathieu, F., Neggers, J., Pled, F., Tomičević, Z., Roux,
2 S., Dec. 2016. Toward 4D mechanical correlation. *Advanced Modeling and Simulation in Engineering*
3 *Sciences* 3 (1).
- 4 Hild, F., Roux, S., May 2006. Digital Image Correlation: From Displacement Measurement to Identification
5 of Elastic Properties - a Review. *Strain* 42 (2), 69–80.
- 6 Hild, F., Roux, S., Nov. 2012. Comparison of Local and Global Approaches to Digital Image Correlation.
7 *Experimental Mechanics* 52 (9), 1503–1519.
- 8 Holzapfel, G. A., 2000. *Nonlinear Solid Mechanics: A Continuum Approach for Engineering*. Wiley, Chich-
9 ester.
- 10 Ibrahim, E.-S. H., Jan. 2011. Myocardial tagging by cardiovascular magnetic resonance: Evolution of tech-
11 niques—pulse sequences, analysis algorithms, and applications. *Journal of cardiovascular magnetic reso-*
12 *nance : official journal of the Society for Cardiovascular Magnetic Resonance* 13 (1), 36.
- 13 Imperiale, A., Chabiniok, R., Moireau, P., Chapelle, D., 2011. Constitutive parameter estimation method-
14 ology using tagged-MRI data. In: *Lecture Notes in Computer Science*. Vol. 6666 LNCS. pp. 409–417.
- 15 Krishnamurthy, A., Villongco, C. T., Chuang, J., Frank, L. R., Nigam, V., Belezouli, E., Stark, P., Krum-
16 men, D. E., Narayan, S. M., Omens, J. H., McCulloch, A. D., Kerckhoffs, R. C. P., Jul. 2013. Patient-
17 Specific Models of Cardiac Biomechanics. *Journal of computational physics* 244, 4–21.
- 18 Le Tallec, P., 1994. Numerical Methods for Nonlinear Elasticity. In: *Handbook of Numerical Analysis*. Vol. 3.
19 pp. 465–622.
- 20 Leclerc, H., Périé, J.-N., Roux, S., Hild, F., 2010. Voxel-Scale Digital Volume Correlation. *Experimental*
21 *Mechanics* 51 (4), 479–490.
- 22 Lee, L. C., Genet, M., Dang, A. B., Ge, L., Guccione, J. M., Ratcliffe, M. B., May 2014. Applications of
23 computational modeling in cardiac surgery. *Journal of Cardiac Surgery* 29 (3), 293–302.
- 24 Lenoir, N., Bornert, M., Desrues, J., Bésuelle, P., Viggiani, G., Aug. 2007. Volumetric Digital Image Corre-
25 lation Applied to X-ray Microtomography Images from Triaxial Compression Tests on Argillaceous Rock.
26 *Strain* 43 (3), 193–205.
- 27 Logg, A., Mardal, K.-A., Wells, G. (Eds.), 2012. Automated Solution of Differential Equations by the Finite
28 Element Method: The FEniCS Book. No. 84 in *Lecture Notes in Computational Science and Engineering*.
29 Springer, Heidelberg.
- 30 Mansi, T., Pennec, X., Sermesant, M., Delingette, H., Ayache, N., Mar. 2011. iLogDemons: A Demons-Based
31 Registration Algorithm for Tracking Incompressible Elastic Biological Tissues. *International Journal of*
32 *Computer Vision* 92 (1), 92–111.
- 33 May-Newman, K., Omens, J. H., Pavelec, R. S., McCulloch, A. D., 1994. Three-dimensional transmural
34 mechanical interaction between the coronary vasculature and passive myocardium in the dog. *Circulation*
35 *Research* 74 (6), 1166–1178.
- 36 McLeod, K., Prakosa, A., Mansi, T., Sermesant, M., Pennec, X., 2012. An Incompressible Log-Domain
37 Demons Algorithm for Tracking Heart Tissue. In: *Statistical Atlases and Computational Models of the*
38 *Heart - Imaging and Modelling Challenges*. pp. 55–67.
- 39 Moireau, P., Chapelle, D., Le Tallec, P., Jan. 2008. Joint state and parameter estimation for distributed
40 mechanical systems. *Computer Methods in Applied Mechanics and Engineering* 197 (6-8), 659–677.
- 41 Moore, C. C., Lugo-Olivieri, C. H., McVeigh, E. R., Zerhouni, E. A., Feb. 2000. Three-dimensional systolic
42 strain patterns in the normal human left ventricle: Characterization with tagged MR imaging. *Radiology*
43 214 (2), 453–466.
- 44 Osman, N. F., Kerwin, W. S., McVeigh, E. R., Prince, J. L., Dec. 1999. Cardiac motion tracking using CINE
45 harmonic phase (HARP) magnetic resonance imaging. *Magnetic Resonance in Medicine* 42 (6), 1048–60.
- 46 Passieux, J.-C., Périé, J.-N., Nov. 2012. High resolution digital image correlation using proper generalized
47 decomposition: PGD-DIC. *International Journal for Numerical Methods in Engineering* 92 (6), 531–550.
- 48 Phatak, N. S., Maas, S. A., Veress, A. I., Pack, N. A., Di Bella, E. V. R., Weiss, J. A., Apr. 2009.
49 Strain measurement in the left ventricle during systole with deformable image registration. *Medical image*
50 *analysis* 13 (2), 354–61.
- 51 Pierré, J.-E., Passieux, J.-C., Périé, J.-N., Bugarin, F., Robert, L., Feb. 2016. Unstructured finite element-

1 based digital image correlation with enhanced management of quadrature and lens distortions. *Optics*
2 *and Lasers in Engineering* 77, 44–53.

3 Press, W. H., Teukolsky, S. A., Vetterling, W. T., Flannery, B. P., 2007. *Numerical Recipes: The Art of*
4 *Scientific Computing*, 3rd Edition. Cambridge University Press, Cambridge, UK ; New York.

5 Remacle, J.-F., Geuzaine, C., Compère, G., Marchandise, E., 2010. High-quality surface remeshing using
6 harmonic maps. *International Journal for Numerical Methods in Engineering*.

7 Rutz, A. K., Ryf, S., Plein, S., Boesiger, P., Kozerke, S., Apr. 2008. Accelerated whole-heart 3D CSPAMM
8 for myocardial motion quantification. *Magnetic resonance in medicine* 59 (4), 755–63.

9 Ryf, S., Spiegel, M. A., Gerber, M., Boesiger, P., Sep. 2002. Myocardial tagging with 3D-CSPAMM. *Journal*
10 *of Magnetic Resonance Imaging* 16 (3), 320–325.

11 Sainte-Marie, J., Chapelle, D., Cimrman, R., Sorine, M., Nov. 2006. Modeling and estimation of the cardiac
12 electromechanical activity. *Computers & Structures* 84 (28), 1743–1759.

13 Schroeder, W., Martin, K., Lorensen, B., 2006. *The Visualization Toolkit: An Object-Oriented Approach*
14 *to 3D Graphics*, 4th Edition. Kitware, Inc, Clifton Park, NY.

15 Sermesant, M., Moireau, P., Camara, O., Sainte-Marie, J., Andriantsimiavona, R., Cimrman, R., Hill, D.
16 L. G., Chapelle, D., Razavi, R., 2006. Cardiac function estimation from MRI using a heart model and
17 data assimilation: Advances and difficulties. *Medical Image Analysis* 10, 642–656.

18 Shehata, M. L., Cheng, S., Osman, N. F., Bluemke, D. A., Lima, J. A., 2009. Myocardial tissue tagging
19 with cardiovascular magnetic resonance. *Journal of Cardiovascular Magnetic Resonance* 11 (1), 55.

20 Sotiras, A., Davatzikos, C., Paragios, N., Jul. 2013. Deformable Medical Image Registration: A Survey.
21 *IEEE Transactions on Medical Imaging* 32 (7), 1153–1190.

22 Stoeck, C. T., Manka, R., Boesiger, P., Kozerke, S., 2012. Undersampled Cine 3D tagging for rapid assess-
23 ment of cardiac motion. *Journal of Cardiovascular Magnetic Resonance* 14 (1), 60.

24 Stoeck, C. T., von Deuster, C., Genet, M., Atkinson, D., Kozerke, S., 2015. Second-order motion-
25 compensated spin echo diffusion tensor imaging of the human heart. *Magnetic Resonance in Medicine*.

26 Sutton, M. A., Hild, F., Jan. 2015. Recent Advances and Perspectives in Digital Image Correlation. *Exper-*
27 *imental Mechanics* 55 (1), 1–8.

28 Thirion, J.-P., Sep. 1998. Image matching as a diffusion process: An analogy with Maxwell’s demons. *Medical*
29 *Image Analysis* 2 (3), 243–260.

30 Tobon-Gomez, C., De Craene, M., McLeod, K., Tautz, L., Shi, W., Hennemuth, A., Prakosa, A., Wang,
31 H., Carr-White, G. S., Kapetanakis, S., Lutz, A., Rasche, V., Schaeffter, T., Butakoff, C., Friman, O.,
32 Mansi, T., Sermesant, M., Zhuang, X., Ourselin, S., Peitgen, H.-O., Pennec, X., Razavi, R., Rueckert, D.,
33 Frangi, A. F., Rhode, K. S., Aug. 2013. Benchmarking framework for myocardial tracking and deformation
34 algorithms: An open access database. *Medical Image Analysis* 17 (6), 632–648.

35 Vercauteren, T., Pennec, X., Perchant, A., Ayache, N., 2008. Symmetric Log-Domain Diffeomorphic Reg-
36 istration: A Demons-Based Approach. In: Metaxas, D., Axel, L., Fichtinger, G., Székely, G. (Eds.),
37 *Medical Image Computing and Computer-Assisted Intervention — MICCAI 2008*. Vol. 5241. Springer
38 Berlin Heidelberg, Berlin, Heidelberg, pp. 754–761.

39 Veress, A. I., Gullberg, G. T., Weiss, J. A., Jul. 2005. Measurement of Strain in the Left Ventricle dur-
40 ing Diastole with cine-MRI and Deformable Image Registration. *Journal of Biomechanical Engineering*
41 127 (7), 1195.

42 von Deuster, C., Stoeck, C. T., Genet, M., Atkinson, D., Kozerke, S., 2015. Spin echo versus stimulated
43 echo diffusion tensor imaging of the in vivo human heart. *Magnetic Resonance in Medicine*.

44 Wang, H., Amini, A. A., 2012. Cardiac motion and deformation recovery from MRI: A review. *IEEE*
45 *transactions on medical imaging* 31 (2), 487–503.

46 Wang, H., Stoeck, C. T., Kozerke, S., Amini, A. A., Jan. 2013. Analysis of 3D cardiac deformations with
47 3D SinMod. *Annual International Conference of the IEEE Engineering in Medicine and Biology Society*
48 2013, 4386–9.

49 Zerhouni, E. A., Parish, D. M., Rogers, W. J., Yang, A., Shapiro, E. P., Oct. 1988. Human heart: Tagging
50 with MR imaging—a method for noninvasive assessment of myocardial motion. *Radiology* 169 (1), 59–63.

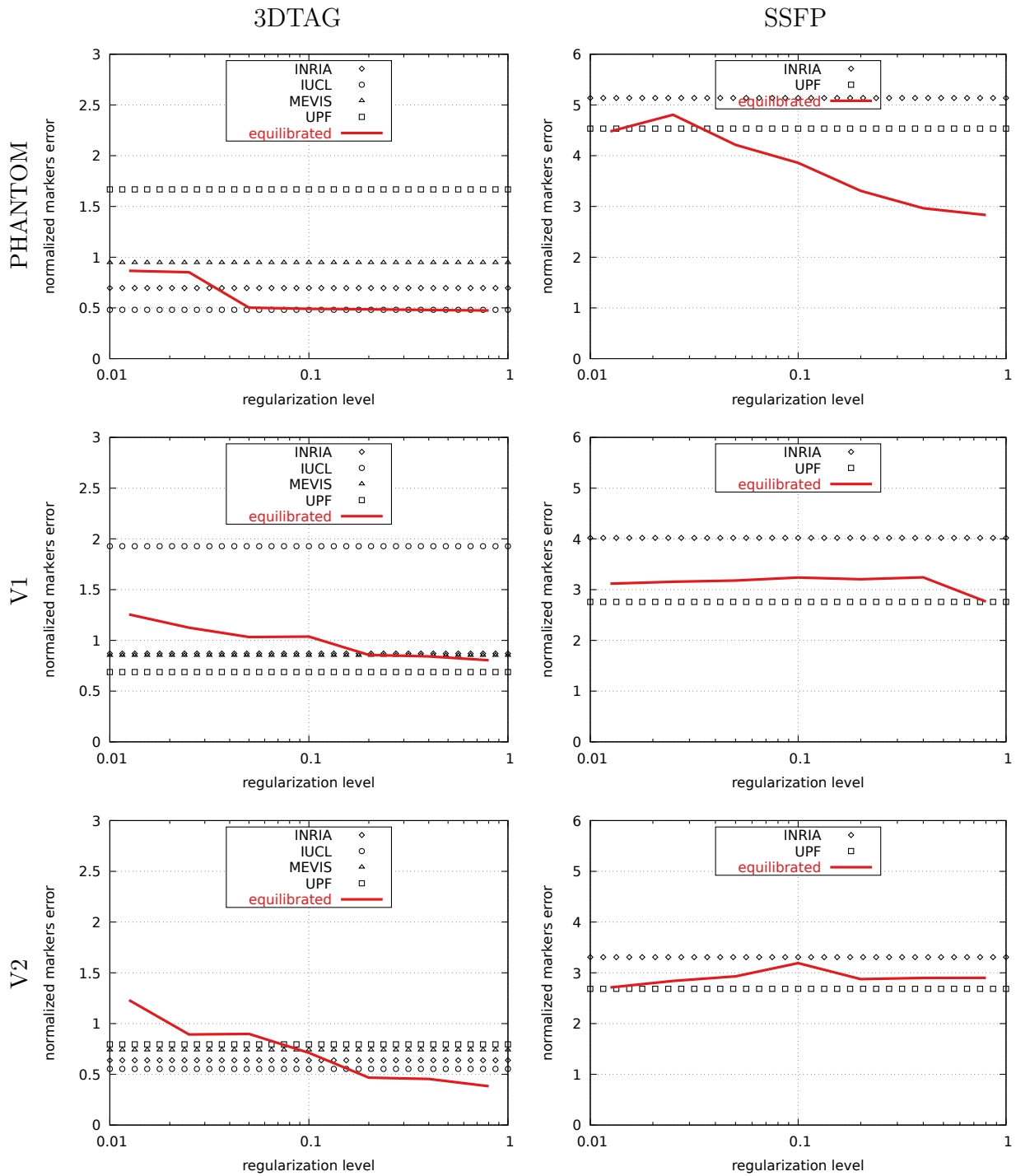


Figure A.1: Validation using Motion Tracking Challenge. Normalized markers error as a function of regularization strength, compared to results obtained by challengers, for 3DTAG & SSFP images, for all cases. One can see that the equilibrium gap regularization is robust, and that the registration is not critically dependent on regularization strength, which can then be roughly determined.

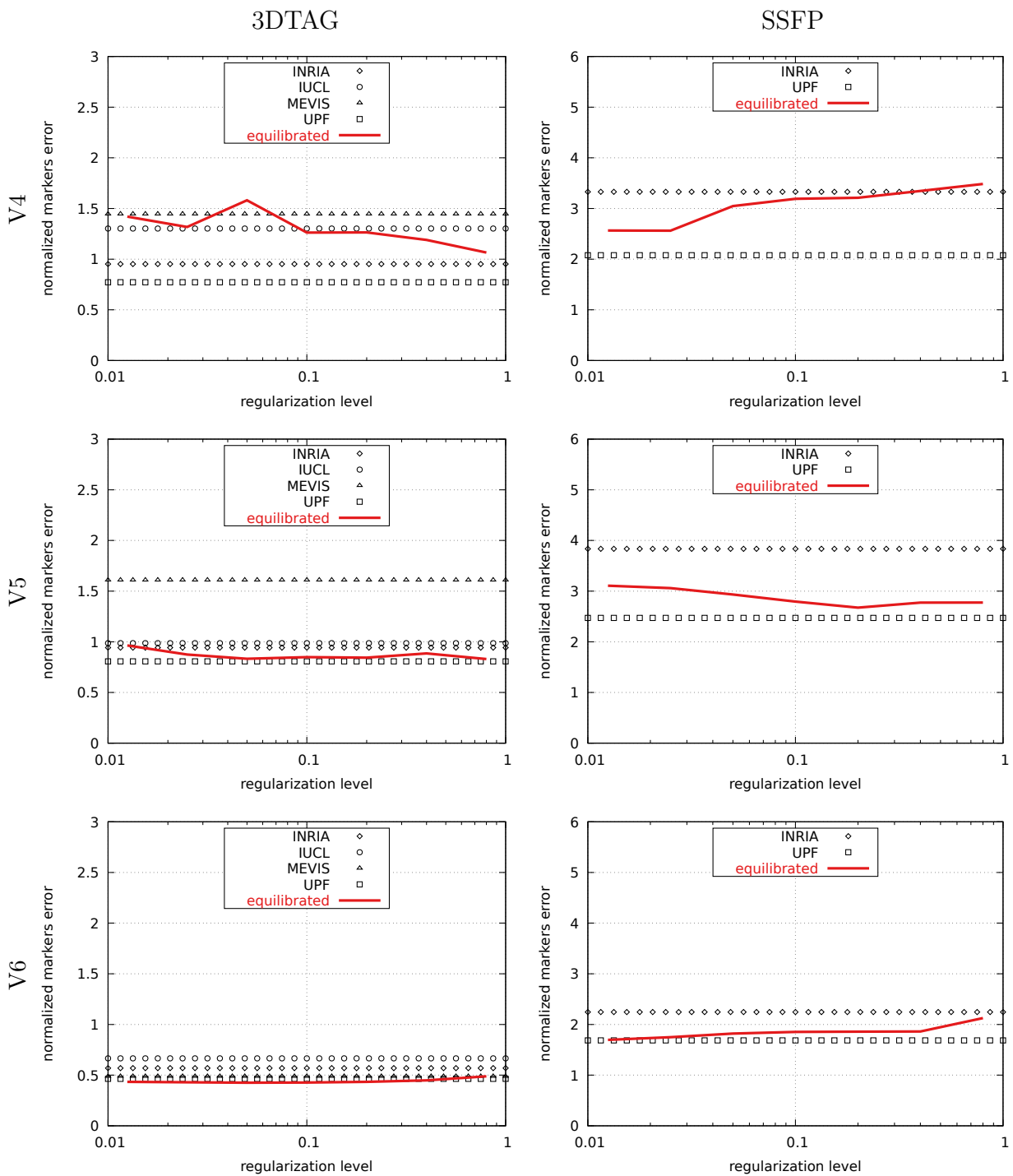


Figure A.1: (Cont.)

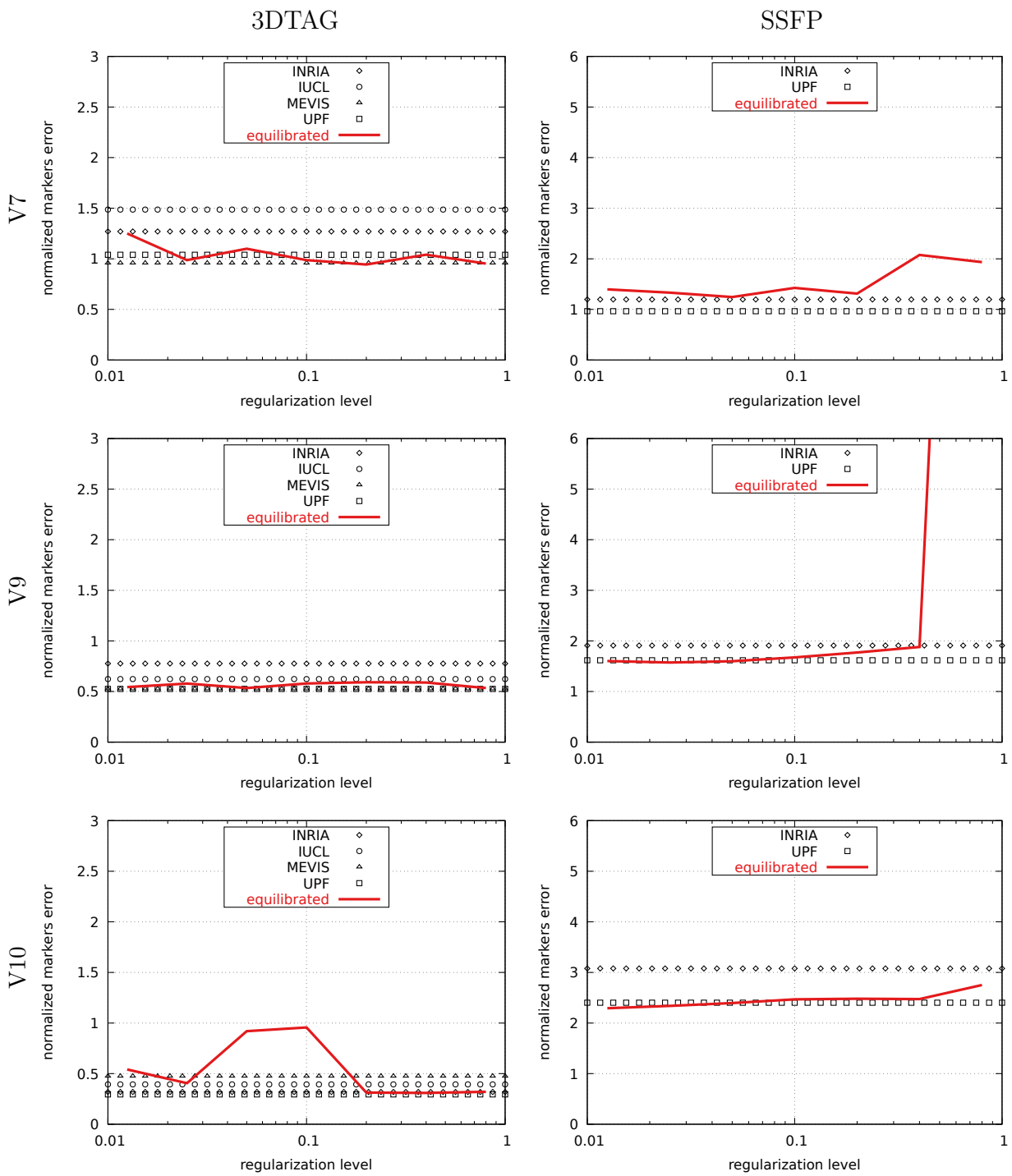


Figure A.1: (Cont.)

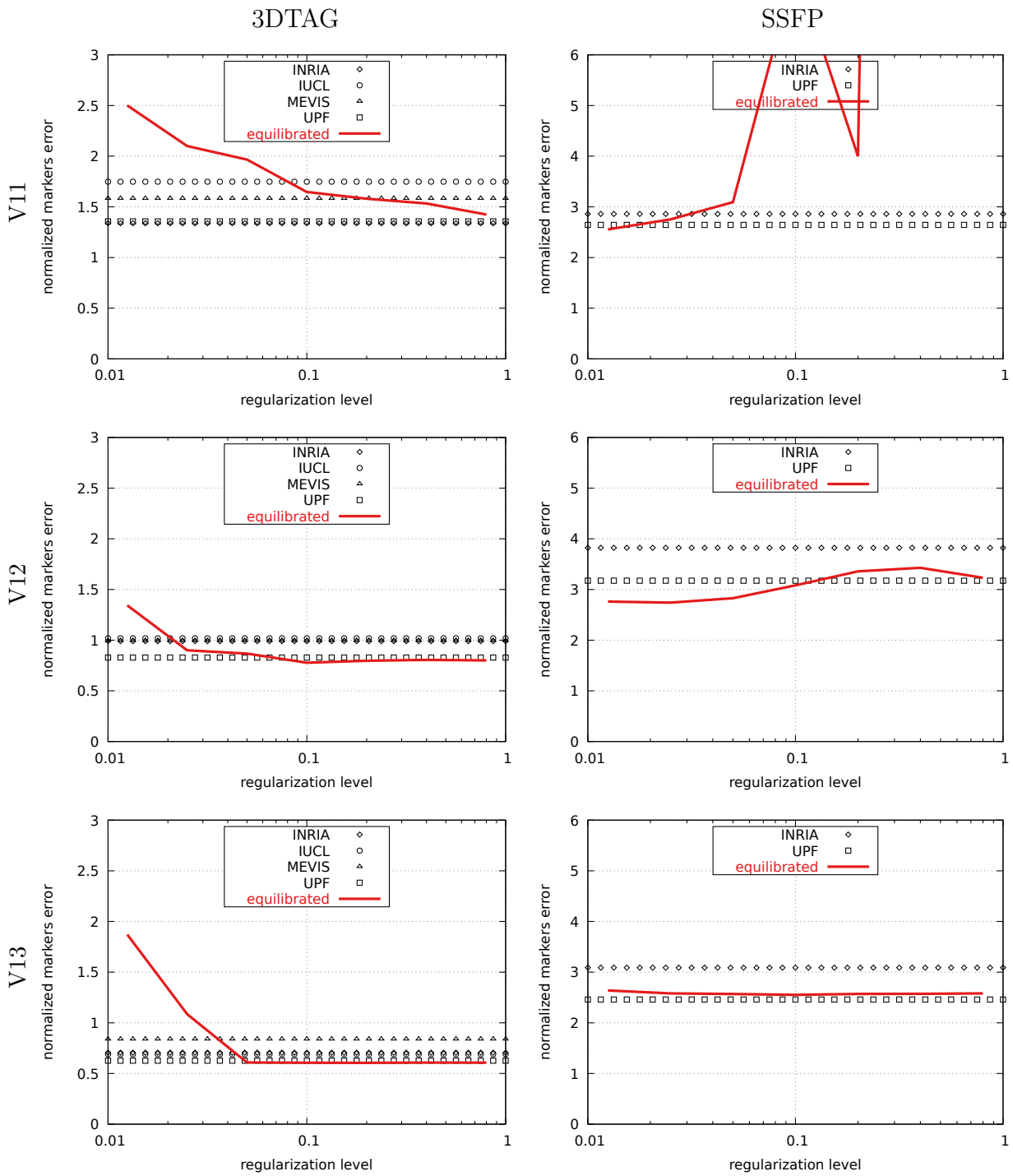


Figure A.1: (Cont.)

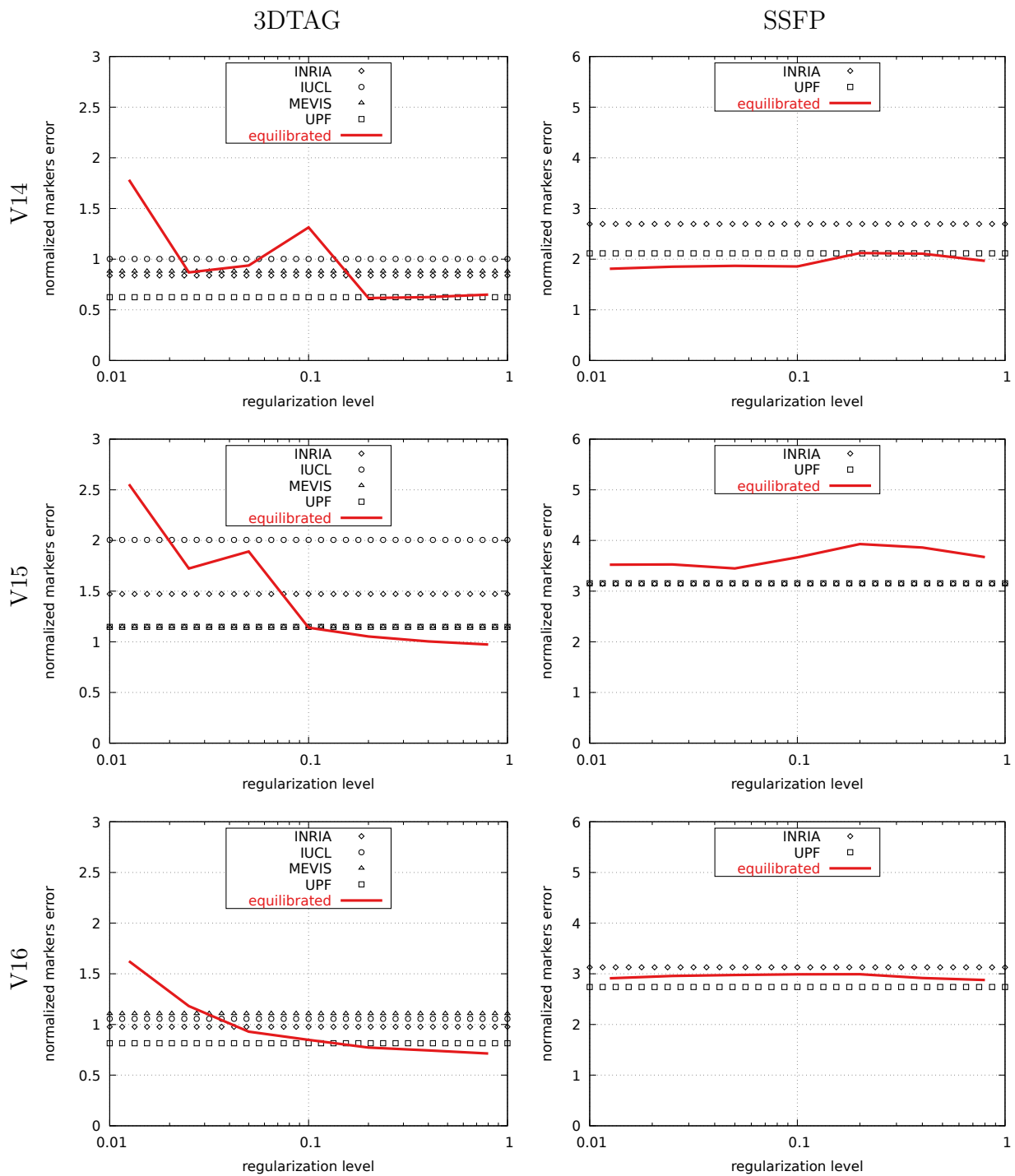


Figure A.1: (Cont.)

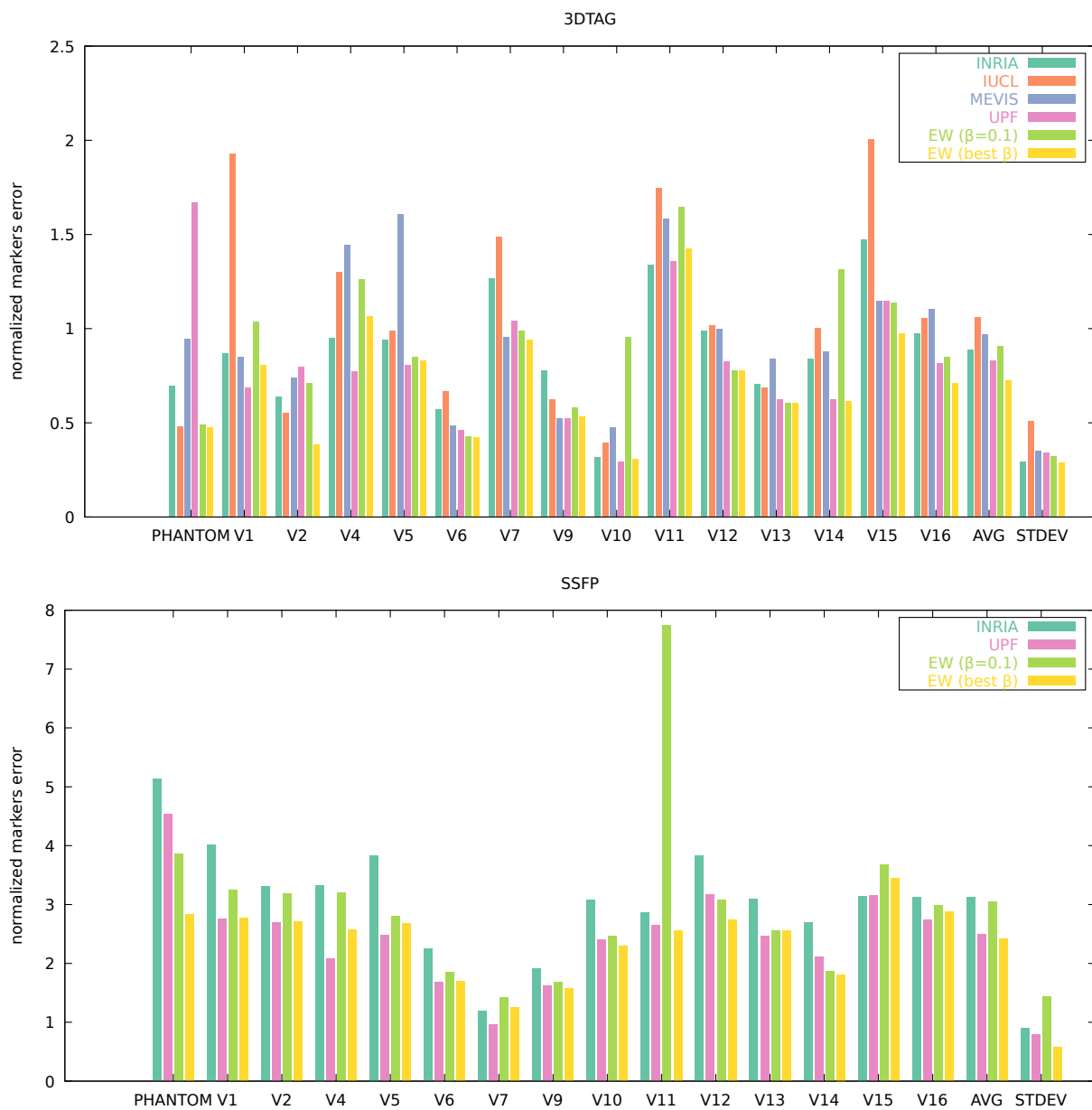


Figure A.2: Validation using Motion Tracking Challenge. Normalized markers error, for both 3DTAG & SSFP images and for all cases, as well as normalized markers error mean and standard deviation over all cases. One can see that the proposed method compares well to the other established registration methods.